

<sup>1</sup>  
<sup>2</sup> Susceptible host dynamics explain pathogen resilience to  
<sup>3</sup> perturbations

<sup>4</sup>

## <sup>5</sup> **Abstract**

<sup>6</sup> A major priority for epidemiological research in the time of anthropogenic change  
<sup>7</sup> is understanding how infectious disease dynamics respond to perturbations. Inter-  
<sup>8</sup> ventions to slow the spread of SARS-CoV-2 significantly disrupted the transmission  
<sup>9</sup> of other human pathogens. As interventions lifted, whether and when respiratory  
<sup>10</sup> pathogens would eventually return to their pre-pandemic dynamics remains to be  
<sup>11</sup> answered. Here, we present a framework for estimating pathogen resilience based on  
<sup>12</sup> how fast epidemic patterns return to their pre-pandemic, endemic dynamics and an-  
<sup>13</sup> alyze time series data from Hong Kong, Canada, Korea, and the US. By quantifying  
<sup>14</sup> the resilience of common respiratory pathogens, we are able to predict when each  
<sup>15</sup> pathogen will eventually return to its pre-pandemic, endemic dynamics. Our pre-  
<sup>16</sup> dictions closely match the observed deviations (or lack thereof) from its pre-COVID  
<sup>17</sup> dynamics. Discrepancies between predicted and observed dynamics indicate the  
<sup>18</sup> long-term impact of pandemic perturbations, suggesting that some pathogens may  
<sup>19</sup> be converging to a different endemic cycle. Finally, we show that the replenishment  
<sup>20</sup> rate of the susceptible pool is a key determinant of pathogen resilience, which in  
<sup>21</sup> turn determines the sensitivity of a system to stochastic perturbations. Overall, our  
<sup>22</sup> analysis highlights the persistent nature of common respiratory pathogens compared  
<sup>23</sup> to vaccine-preventable infections, such as measles.

24 Non-pharmaceutical interventions to slow the spread of SARS-CoV-2 disrupted  
 25 the transmission of other human respiratory pathogens, adding uncertainties to their  
 26 future epidemic dynamics and their public health burden [1]. As interventions lifted,  
 27 large heterogeneities in outbreak dynamics were observed across different pathogens  
 28 in different countries, with some pathogens exhibiting earlier and faster resurgences  
 29 than others [2, 3, 4]. Heterogeneities in the overall reduction in transmission and the  
 30 timing of re-emergence likely reflect differences in intervention patterns, pathogen  
 31 characteristics, immigration/importation from other countries, and pre-pandemic  
 32 pathogen dynamics [5]. Therefore, comparing the differential impact of the pan-  
 33 demic perturbations across pathogens can provide unique opportunities to learn  
 34 about underlying pathogen characteristics, such as their transmissibility or duration  
 35 of immunity, from heterogeneities in re-emergence patterns [6].

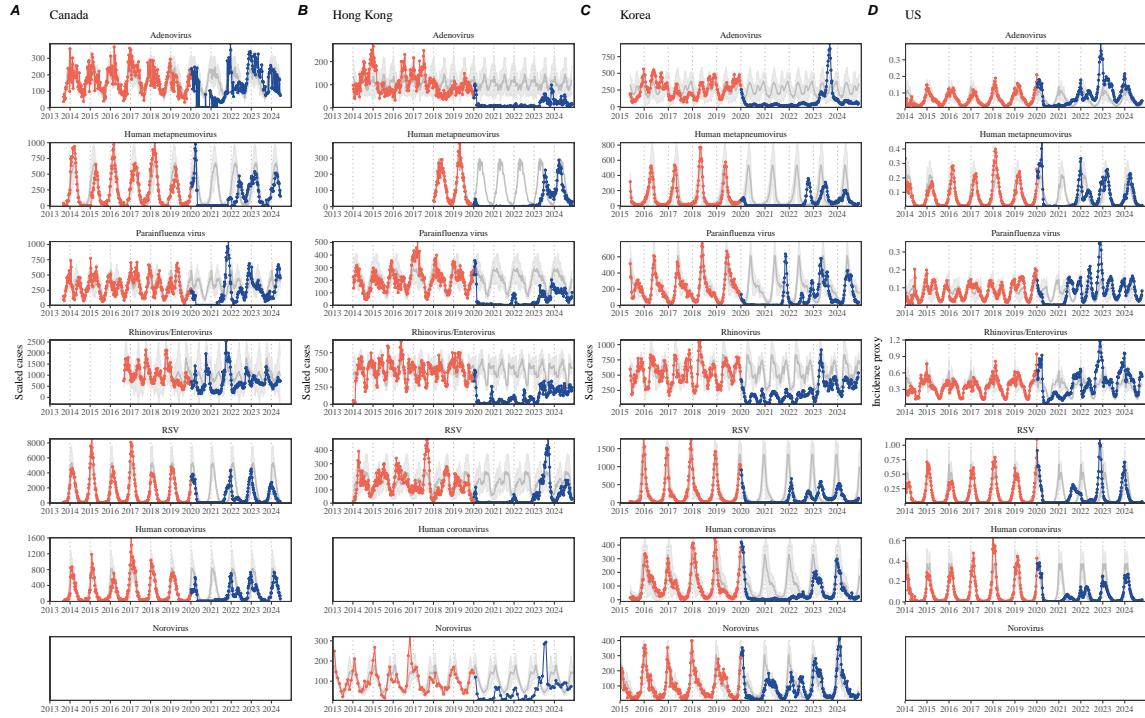


**Figure 1: Observed heterogeneity in responses to pandemic perturbations across respiratory pathogens and norovirus in (A) Canada, (B) Hong Kong, (C) Korea, and (D) US.** Red points and lines represent data before 2020. Blue points and lines represent data since 2020. Gray lines and shaded regions represent the mean seasonal patterns and corresponding 95% confidence intervals around the mean. Mean seasonal patterns were calculated by aggregating cases before 2020 into 52 weekly bins and taking the average in each week. Cases were scaled to account for changes in testing patterns (Materials and Methods).

36 Even though more than five years have passed since the emergence of SARS-CoV-  
 37 2, we still observe persistent changes in pathogen dynamics following the pandemic

38 perturbations. For example, compared to pre-pandemic, seasonal patterns, human  
39 metapneumovirus in Korea seem to circulate at lower levels, whereas RSV in Korea  
40 seems to exhibit different seasonality (Figure 1). These observations suggest a funda-  
41 mental change in pathogen dynamics following the pandemic perturbations, which  
42 might be driven by a long-term shift in either human behavior or population-level  
43 immunity [7, 8]. For example, the emergence of SARS-CoV-2 could have caused  
44 a long-term shift in population-level immunity through its interactions with other  
45 pathogens [9], especially with seasonal coronaviruses [7, 10, 11]. The possibility of a  
46 long-lasting impact of the pandemic perturbations poses an important question for  
47 future infectious disease dynamics: can we predict whether and when other pathogens  
48 will eventually return to their pre-pandemic dynamics?

49 So far, most analyses of respiratory pathogens after pandemic perturbations have  
50 focused on characterizing the timing of rebound [1, 12, 5]. Instead, we seek to char-  
51 acterize how fast (and whether) a pathogen returns to its pre-pandemic dynamics.  
52 These two concepts have a subtle but important difference. For example, it took  
53 more than 3 years for human metapneumovirus to rebound in Hong Kong, but the  
54 observed epidemic patterns in 2024 are similar to pre-pandemic seasonal means, sug-  
55 gesting a rapid return to pre-pandemic dynamics (Figure 1). Measuring this rate of  
56 return is useful because it allows us to quantify the ecological resilience of a host-  
57 pathogen system, which can inform responses to future interventions [13, 14, 15, 16].

58 In this study, we lay out theoretical and statistical approaches to characterizing  
59 the resilience of a host-pathogen system based on how fast the system recovers from  
60 perturbation. We begin by laying out a few representative scenarios that capture the  
61 potential impact of pandemic perturbations on endemic pathogen dynamics and illus-  
62 trate how resilience can be measured by comparing the pre- and post-pandemic dy-  
63 namics of susceptible and infected hosts. In practice, information on susceptible hosts  
64 is often unavailable, making this theoretical approach infeasible. Instead, we utilize a  
65 mathematical technique to reconstruct empirical attractors from the data [17], which  
66 allows us to measure the rate at which the host-pathogen system approaches this em-  
67 pirical attractor after a perturbation; this rate corresponds to the resilience of the  
68 host-pathogen system. We use this method to analyze pathogen surveillance data for  
69 respiratory and non-respiratory pathogens from Canada, Hong Kong, Korea, and the  
70 US. Finally, we show that susceptible host dynamics explain variation in pathogen  
71 resilience and further demonstrate that more resilient pathogens will be less sensitive  
72 to perturbations caused by demographic stochasticity, thereby providing a direct link  
73 between pathogen resilience and persistence.

## 74 **Conceptual introduction to pathogen resilience**

75 In classical ecological literature, the resilience of an ecological system is measured by  
76 the rate at which the system returns to its reference state following a perturbation  
77 [13, 14, 15, 16]. This rate corresponds to the largest real part of the eigenvalues of

78 the linearized system near equilibrium—here, we refer to this value as the *intrinsic*  
79 resilience of the system, which represents the expected rate of return from perturbed  
80 states. In practice, we rarely know the true model describing population-level dy-  
81 namics of common respiratory pathogens, limiting our ability to infer the intrinsic  
82 resilience of a system. Instead, we can still measure the *empirical* resilience of a  
83 host-pathogen system by looking at how fast the system returns to the pre-pandemic,  
84 endemic dynamics after pandemic perturbations are lifted.

85 As an example, we begin with a simple Susceptible-Infected-Recovered-Susceptible  
86 (SIRS) model with seasonally forced transmission and demography (i.e., birth and  
87 death). The SIRS model is the simplest model that allows for the waning of im-  
88 munity and is commonly used for modeling the dynamics of respiratory pathogens  
89 [18]. First, consider a pandemic perturbation that reduces transmission by 50% for 6  
90 months starting in 2020, which causes epidemic patterns to deviate from their origi-  
91 nal stable annual cycle for a short period of time and eventually come back (Figure  
92 2A). To measure the resilience of this system empirically, we first need to be able to  
93 measure the distance from its pre-pandemic attractor. There are many ways we can  
94 measure the distance from the attractor, but for illustrative purposes, we choose one  
95 of the most parsimonious approaches: that is, we look at how the susceptible (S) and  
96 infected (I) populations change over time and measure the distance on the SI phase  
97 plane (Figure 2B). In this simple case, the locally estimated scatterplot smoothing  
98 (LOESS) fit indicates that the distance from the attractor decreases exponentially  
99 (linearly on a log scale) on average (Figure 2C). Furthermore, the overall rate of re-  
100 turn approximates the intrinsic resilience of the seasonally unforced system (Figure  
101 2C).

102 Alternatively, pandemic perturbations can have a lasting impact on the pathogen  
103 dynamics; as an example, we consider a scenario in which a 10% reduction in trans-  
104 mission persists even after the major pandemic perturbations are lifted (Figure 2D–  
105 F). In such cases, we cannot know whether the pathogen will return to its original  
106 cycle or a different cycle until many years have passed, and we cannot measure the  
107 distance to the new unknown attractor that the system might eventually approach.  
108 Nonetheless, we can still measure the distance from the pre-pandemic attractor and  
109 ask how the distance changes over time (Figure 2E). The LOESS fit suggests that the  
110 distance from the pre-pandemic attractor will initially decrease exponentially on av-  
111 erage (equivalently, linearly on a log scale) and eventually plateau (Figure 2F). Here,  
112 a permanent 10% reduction in transmission rate slows the system, which causes the  
113 distance from the pre-pandemic attractor initially to decrease at a slower rate (Figure  
114 2F) than it would have otherwise (Figure 2C) before plateauing at a fixed distance  
115 between the two attractors. This example shows that resilience is not necessarily an  
116 intrinsic property of a specific pathogen. Instead, pathogen resilience is a property  
117 of a specific attractor that a host-pathogen system approaches, which depends on  
118 both pathogen and host characteristics.

119 Finally, transient phenomena can further complicate the picture (Figure 2G–I).  
120 For example, a stage-structured model initially exhibits a stable annual cycle, but

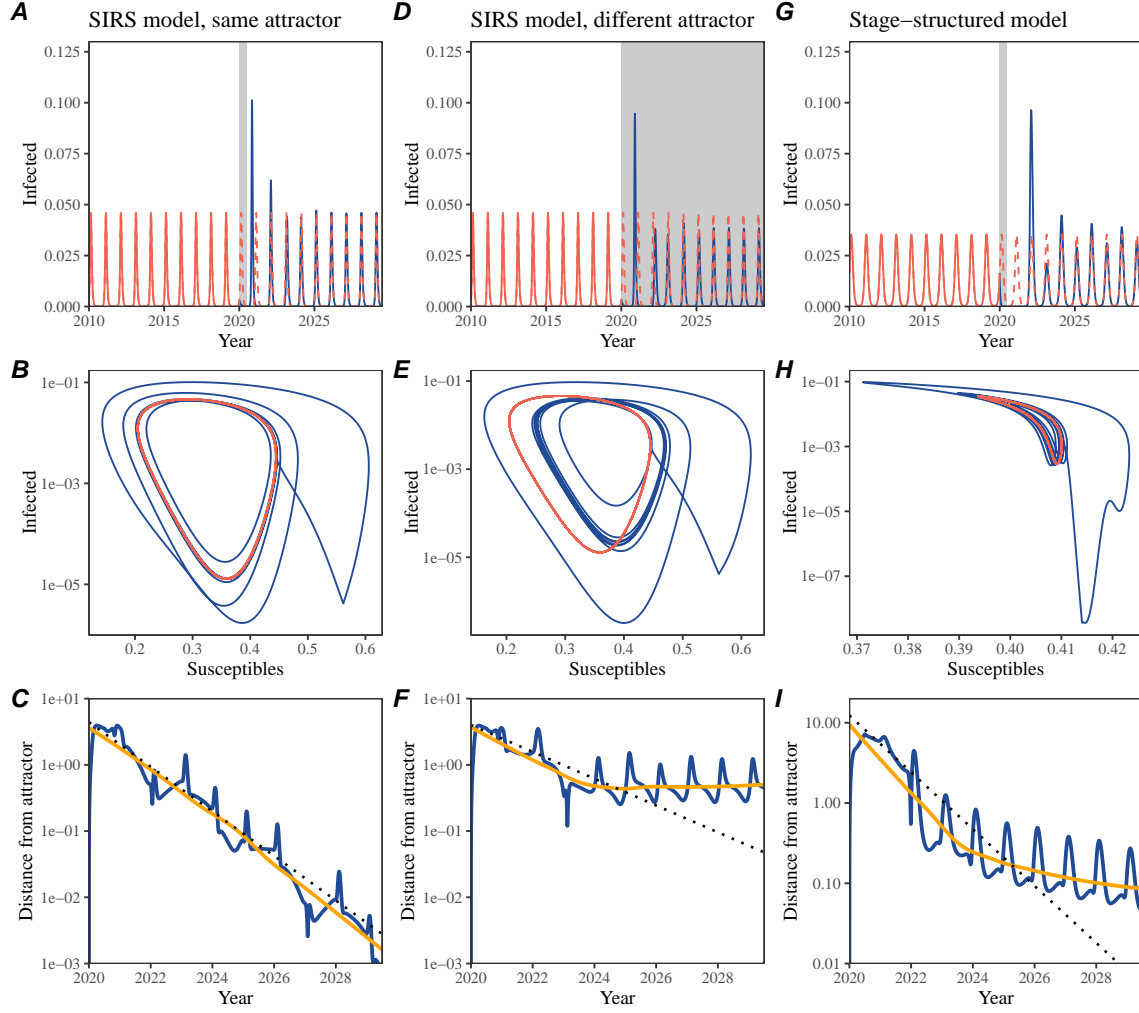


**Figure 2: A simple method to measure pathogen resilience following pandemic perturbations across different scenarios.** (A, D, G) Simulated epidemic trajectories across various models. Red and blue solid lines represent epidemic dynamics before and after pandemic perturbations are introduced, respectively. Red dashed lines represent counterfactual epidemic dynamics in the absence of perturbations. Gray regions indicate the duration of perturbations. (B, E, H) Phase plane representation of the time series in panels A, D, and G alongside the corresponding susceptible host dynamics. Red and blue solid lines represent epidemic trajectories on an SI phase plane before and after perturbations are introduced, respectively. (C, F, I) Changes in logged distance from the attractor over time. Blue lines represent the logged distance from the attractor. Orange lines represent the locally estimated scatterplot smoothing (LOESS) fits to the logged distance from the attractor. Dotted lines show the intrinsic resilience of the seasonally unforced system.

121 perturbations from a 10% reduction in transmission for 6 months cause the epidemic

122 to shift to biennial cycles (Figure 2G). The system eventually approaches the original  
123 pre-pandemic attractor (Figure 2H), suggesting that this biennial cycle is a transient  
124 phenomenon. The LOESS fit indicates that the distance from the attractor initially  
125 decreases exponentially at a rate that is consistent with the intrinsic resilience of  
126 the seasonally unforced stage-structured system, but the rate of decrease decelerates  
127 with the damped oscillations (Figure 2I). This behavior is also referred to as a ghost  
128 attractor, which causes long transient dynamics and slow transitions [19]. Strong  
129 seasonal forcing in transmission can also lead to transient phenomena for a simple  
130 SIRS model, causing a slow return to pre-perturbation dynamics (Supplementary  
131 Figure S1).

132 This empirical approach allows us to measure the resilience of a two-strain host-  
133 pathogen system even when we have incomplete observation of the infection dynam-  
134 ics. Simulations from a simple two-strain competition system illustrate that separate  
135 analyses of individual strain dynamics (e.g., RSV A vs B) and a joint analysis of total  
136 infections (e.g., total RSV infections) yield identical resilience estimates (Supplemen-  
137 tary Figure S2, 3). This is expected because the dynamics of two strains (or two  
138 pathogens) around the attractor in a coupled system are described by the same set  
139 of eigenvalues and eigenvectors, meaning that both strains should exhibit identical  
140 rates of returns following a perturbation. Analogous to a single system, strong sea-  
141 sonal forcing in transmission can cause the system to slow down through transient  
142 phenomena (Supplementary Figure S4).

143 These observations yield three insights. First, we can directly estimate the empirical  
144 resilience of a host-pathogen system by measuring the rate at which the system  
145 approaches an attractor, provided that we have a way to quantify the distance from  
146 the attractor. The empirical approach to estimating pathogen resilience is particu-  
147 larly convenient because it does not require us to know the true underlying model;  
148 estimating the intrinsic resilience from fitting misspecified models can lead to biased  
149 estimates (Supplementary Figure S5). Second, resilience estimates allow us to make  
150 phenomenological predictions about the dynamics of a host-pathogen system follow-  
151 ing a perturbation. Assuming that an attractor has not changed and the distance  
152 from the attractor will decrease exponentially over time, we can obtain a ballpark  
153 estimate for when the system should reach an attractor. Finally, a change in the rate  
154 of an exponential decrease in the distance from the attractor can provide information  
155 about whether the system has reached an alternative attractor, or a ghost attractor,  
156 that is different from the original, pre-pandemic attractor. These alternative attrac-  
157 tors may reflect continued perturbations from permanent changes in transmission  
158 patterns as well as changes in immune landscapes. There will be periods of time  
159 when it is difficult to tell whether pathogen dynamics are still diverging from the  
160 original attractor or have begun to converge to a new attractor; now that several  
161 years have passed since interventions have been lifted, we expect many respiratory  
162 pathogens to have had sufficient time to begin returning to their post-intervention  
163 attractors. With recent data, we can start to evaluate whether we see early signs of  
164 convergence to the former attractor or a new one.

165 **Inferring pathogen resilience from real data**

166 Based on these observations, we now lay out our approach to estimating pathogen  
167 resilience from real data (Figure 3). We first tested this approach against simulations  
168 and applied it to real data. Specifically, we analyzed case time series of respiratory  
169 pathogens from four countries: Canada, Hong Kong, Korea, and the US.

170 So far, we have focused on simple examples that assume a constant transmission  
171 reduction during the pandemic. However, in practice, the impact of pandemic per-  
172 turbations on pathogen transmission was likely more complex (Figure 3A), reflecting  
173 introduction and relaxation of various intervention strategies. In some cases, strong  
174 perturbations likely caused local fadeouts, requiring immigration from another loca-  
175 tion for epidemic rebound. Such complexities could lead to longer delays between  
176 the introduction of pandemic perturbations and pathogen rebound as well as tempo-  
177 ral variation in outbreak sizes (Figure 3B): in this example, continued transmission  
178 reduction from interventions limits the size of the first outbreak in 2021 following  
179 the rebound, allowing for a larger outbreak in 2022 when interventions are further  
180 relaxed.

181 Previously, we relied on the dynamics of susceptible and infected hosts to com-  
182 pute the distance from the attractor (Figure 2), but information on susceptible hosts  
183 is rarely available in practice. In addition, uncertainties in case counts due to ob-  
184 servation error, strain evolution, and multiannual cycles in the observed epidemic  
185 dynamics (e.g., adenovirus circulation patterns in Hong Kong and Korea) add chal-  
186 lenges to defining pre-pandemic attractors, which limits our ability to measure the  
187 distance from the attractor. To address these challenges, we can reconstruct an em-  
188 pirical attractor by utilizing Takens' theorem [17], which states that an attractor of a  
189 nonlinear multidimensional system can be mapped onto a delayed embedding (Mate-  
190 rials and Methods). For example, we can use delayed logged values of pre-pandemic  
191 cases  $C(t)$  (Figure 3C) to reconstruct the attractor:

$$\langle \log(C(t) + 1), \log(C(t - \tau) + 1), \dots, \log(C(t - (M - 1)\tau) + 1) \rangle, \quad (1)$$

192 where the delay  $\tau$  and embedding dimension  $M$  are determined based on autocor-  
193 relations and false nearest neighbors, respectively [20, 21]. We can then apply the  
194 same delay and embedding dimensions to the entire time series to determine the po-  
195 sition in multi-dimensional state space (Figure 3D), which allows us to measure the  
196 nearest neighbor distance between the current state of the system and the empirical  
197 pre-pandemic attractor (Figure 3E). In theory, we can now quantify how fast this  
198 distance decreases by fitting a linear regression on a log scale, where the slope of  
199 the linear regression empirically measures pathogen resilience. However, resulting  
200 estimates of pathogen resilience can be sensitive to choices about embedding delays  
201 and dimensions. For example, using longer delays and higher dimensions tends to  
202 smooth out temporal variations in the distance from the attractor (Supplementary  
203 Figure S6).

204 Complex changes in the distance from the attractor suggest that estimating

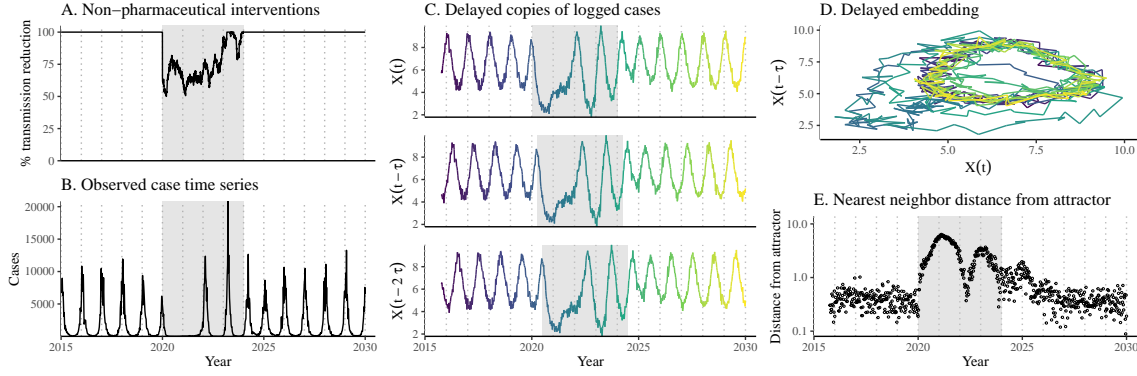


**Figure 3: A schematic diagram explaining the inference of pathogen resilience from synthetic data.** (A) A realistic example of simulated pandemic perturbations, represented by a relative reduction in transmission. (B) The impact of the synthetic pandemic perturbation on epidemic dynamics simulated using a SIRS model with demographic stochasticity. (C) Generating delayed copies of the logged time series allows us to obtain an embedding. (D) Two dimensional representation of an embedding. (E) Delayed embedding allows us to calculate the nearest neighbor distance from the empirical attractor, which is determined based on the pre-pandemic time series. This distance time series can be used to infer pathogen resilience after choosing an appropriate window for linear regression.

pathogen resilience from linear regression will be particularly sensitive to our choice of fitting windows for the regression (Figure 3E). Therefore, before we tried estimating resilience from real data, we explored an automated window selection criterion for linear regression and tested it against randomized, stochastic simulations across a range of realistic pandemic perturbation shapes. In doing so, we also explored optimal choices for embedding dimensions and evaluated our choices of fitting window parameters and embedding dimensions by quantifying correlation coefficients between the estimated resilience and the intrinsic resilience of a seasonally unforced system (Materials and Methods). Overall, we found large variation in estimation performances with correlation coefficient ranging from 0.21 to 0.61 (Supplementary Figure S7). In almost all cases, the automated window selection approach outperformed a naive approach that uses the time series, starting from the peak distance (Supplementary Figure S7).

Based on the best performing window selection criteria and embedding dimension, we applied this approach to pathogen surveillance data presented in Figure 1 (Materials and Methods). For each time series, we applied Takens' theorem independently to reconstruct the empirical attractor and obtained the corresponding time series of distances from attractors (Supplementary Figure S8). Then, we used the automated window selection criterion to fit a linear regression and estimated the empirical resilience for each pathogen in each country (Supplementary Figure S8); the window selection criterion gave poor regression window for three cases (norovirus

226 in Hong Kong and Korea and rhinovirus/enterovirus in the US), leading to unrealistically low resilience estimates, and so we used ad-hoc regression windows instead  
227 (Supplementary Figure S9; Materials and Methods).

228 For all pathogens we considered, resilience estimates fell between 0.4/year and  
229 1.8/year (Figure 4A). We estimated the mean resilience of common respiratory  
230 pathogens to be 0.99/year (95% CI: 0.81/year–1.18/year). For reference, this is  
231  $\approx$  7.5 times higher than the intrinsic resilience of pre-vaccination measles in England  
232 and Wales ( $\approx$  0.13/year). Finally, resilience estimates for norovirus were comparable  
233 to those of common respiratory pathogens: 1.44/year (95%CI: 1.01/year–1.87/year)  
234 for Hong Kong and 1.07/year (95%CI: 0.86/year–1.29/year) for Korea. Based on  
235 a simple ANOVA test, we did not find significant differences in resilience estimates  
236 across countries ( $p = 0.25$ ) or pathogens ( $p = 0.67$ ).

237 Using resilience estimates, we predicted when each pathogen would hypothetically  
238 return to their pre-pandemic dynamics, assuming no long-term change in the attractor.  
239 Specifically, we extended our linear regression fits to distance-from-attractor  
240 time series and ask when the predicted regression line will cross a threshold value;  
241 since we relied on nearest neighbor distances, pre-pandemic distances are always  
242 greater than zero (Figure 3E), meaning that we can use the mean of pre-pandemic  
243 distances as our threshold.

244 We predicted that a return to pre-pandemic cycles has occurred would be im-  
245 minent for most pathogens (Figure 4B). In particular, we predicted that 12 out of  
246 23 pathogen-country pairs should have already returned before the end of 2024. For  
247 almost all pathogens that were predicted to have returned already, the observed  
248 epidemic dynamics showed clear convergence towards their pre-pandemic seasonal  
249 averages, confirming our predictions (Figure 4C). However, there were a few ex-  
250 ceptions, including norovirus in Hong Kong and rhinovirus/enterovirus in the US,  
251 where the observed epidemic dynamics in 2024 exhibit clear deviation from their pre-  
252 pandemic seasonal averages (Figure 4C; Figure S9). These observations suggest a  
253 possibility that some common respiratory pathogens may have converged to different  
254 attractors or are still exhibiting non-equilibrium dynamics. In contrast, pathogens  
255 that were predicted to have not returned yet also showed clear differences from their  
256 pre-pandemic seasonal averages; as many of these pathogens are predicted to return  
257 in 2025–2026, we may be able to test these predictions in near future (Supplementary  
258 Figure S10). Our reconstructions of distance time series and estimates of pathogen  
259 resilience and expected return time were generally robust to choices of embedding  
260 dimensions (Supplementary Figure S11–12).

## 262 Susceptible host dynamics explain variation in pathogen 263 resilience

264 So far, we have focused on quantifying pathogen resilience from the observed pat-  
265 terns of pathogen re-emergence following pandemic perturbations. But what factors

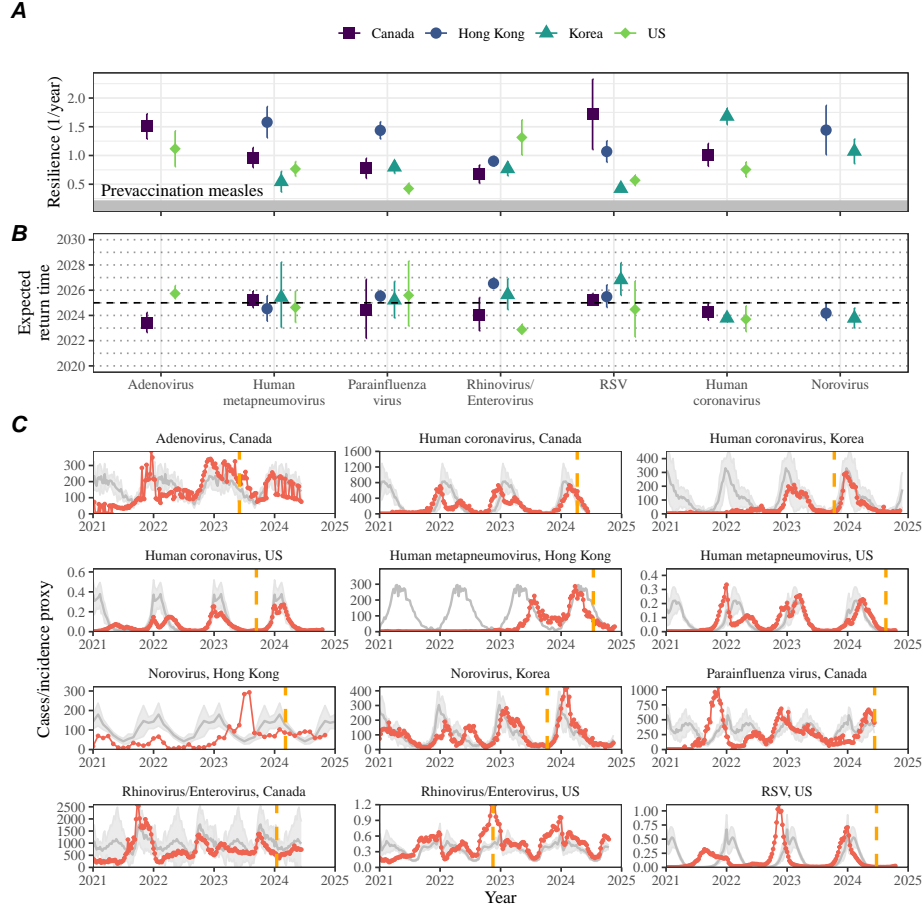
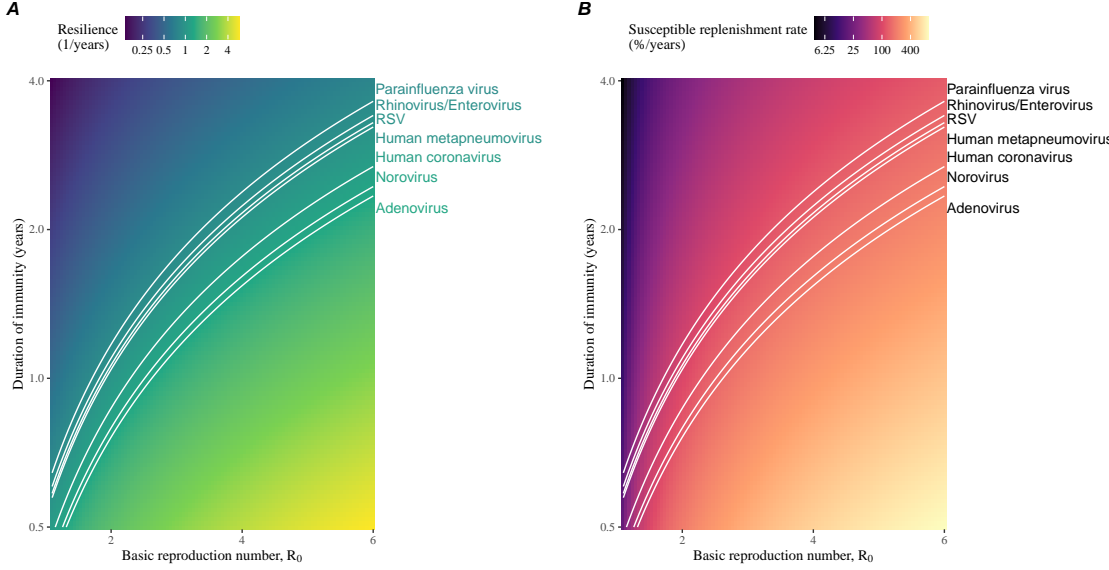


Figure 4: **Summary of resilience estimates and predictions for return time.** (A) Estimated pathogen resilience. The gray horizontal line represents the intrinsic resilience of pre-vaccination measles dynamics. (B) Predicted timing of when each pathogen will return to their pre-pandemic cycles. The dashed line in panel B indicates the end of 2024. Error bars represent 95% confidence intervals. (C) Observed dynamics for pathogen that are predicted to have returned before the end of 2024. Red points and lines represent data before 2020. Gray lines and shaded regions represent the mean seasonal patterns and corresponding 95% confidence intervals around the mean, previously shown in Figure 1. Orange vertical lines represent the predicted timing of return.

determine how resilient a host-pathogen system is? To address this question, we used the SIRS model to explore how changes in susceptible host dynamics affect pathogen resilience. To do so, we varied the basic reproduction number  $\mathcal{R}_0$ , which represents the average number of secondary infections caused by a newly infected individual in a fully susceptible population, and the duration of immunity and computed intrinsic resilience for each parameter.



**Figure 5: Linking pathogen resilience to epidemiological parameters and susceptible host dynamics.** (A) Intrinsic resilience as a function of the basic reproduction number  $\mathcal{R}_0$  and the duration of immunity. (B) Per-capita susceptible replenishment rate as a function of the basic reproduction number  $\mathcal{R}_0$  and the duration of immunity. The standard SIRS model without seasonal forcing is used to compute intrinsic resilience and the per-capita susceptible replenishment rate. Lines correspond to a set of parameters that are consistent with mean resilience estimates for each pathogen, averaged across different countries.

272 We found that an increase in  $\mathcal{R}_0$  and a decrease in the duration of immunity  
 273 correspond to an increase in pathogen resilience (Figure 5A). Similarly, an increase  
 274 in  $\mathcal{R}_0$  and a decrease in the duration of immunity corresponds to a faster per-capita  
 275 rate of susceptible replenishment, which is defined as the ratio between absolute  
 276 rate at which new susceptibles enter the population and the equilibrium number of  
 277 susceptible individuals in the population,  $S^*$  (Figure 5B). We note that a higher  $\mathcal{R}_0$   
 278 drives a faster per-capita susceptible replenishment rate by decreasing the susceptible  
 279 proportion at equilibrium,  $S^*$ . For a simple SIR model that assumes a life-long  
 280 immunity, we can show analytically that pathogen resilience is proportional to the  
 281 per-capita rate of susceptible replenishment (Materials and Methods). Overall, these  
 282 observations suggest that a faster per-capita susceptible replenishment rate causes  
 283 the system to be more resilient.

284 By taking the average values of empirical resilience values for each pathogen, we  
 285 were able to map each pathogen onto a set of parameters of the SIRS model that are  
 286 consistent with corresponding resilience estimates (Figure 5A). Across all pathogens  
 287 we considered, we estimated that the average duration of immunity is likely to be  
 288 short ( $< 4$  years) across a plausible range of  $\mathcal{R}_0$  ( $< 6$ ). We were also able to obtain

<sup>289</sup> a plausible range of susceptible replenishment rates for each pathogen (Figure 5B),  
<sup>290</sup> but there was a large uncertainty in the estimates for susceptible replenishment rates  
<sup>291</sup> due to a lack of one-to-one correspondence between susceptible replenishment rates  
<sup>292</sup> and pathogen resilience.

<sup>293</sup> **Pathogen resilience determines sensitivity to stochastic perturbations**

<sup>295</sup> Beyond the pandemic perturbations, we hypothesized host-pathogen systems to experience continued perturbations of varying degrees from changes in epidemiological conditions, such as human behavior, climate, and viral evolution. These perturbations can also arise from demographic stochasticity, which is inherent to any ecological systems. Here, we used a seasonally unforced SIRS model with birth/death to explore how resilience of a host-pathogen system determines the sensitivity to perturbations caused by demographic stochasticity (Materials and Methods).

<sup>302</sup> We found that resilience of a host-pathogen system determines the amount of deviation from the deterministic trajectory caused by demographic stochasticity, with less resilient systems experiencing larger deviations (Figure 6). Notably, less resilience systems also exhibited slower epidemic cycles (Figure 6A–C). The periodicity of this epidemic cycle matched those predicted by the intrinsic periodicity of the system (Supplementary Figure S13) where the intrinsic resilience of the system is inversely proportional to its intrinsic periodicity (Supplementary Figure S14). We note that the intrinsic resilience is not the sole determinant for how sensitive the system is to stochastic perturbations. For example, the population size and average duration of infection also affect the amount of deviation from the deterministic trajectory caused by demographic stochasticity, even though these quantities have little to no impact on the intrinsic resilience (Supplementary Figure S15). These conclusions were robust for the seasonally forced SIRS model (Supplementary Figure S16).

<sup>315</sup> **Discussion**

<sup>316</sup> COVID-19 pandemic interventions caused major disruptions to circulation patterns of both respiratory and non-respiratory pathogens, adding challenges to predicting their future dynamics [1, 2, 3, 4]. However, these perturbations offer large-scale natural experiments for understanding how different pathogens respond to perturbations.  
<sup>319</sup> In this study, we showed that pathogen re-emergence patterns following pandemic perturbations can be characterized through the lens of ecological resilience. We showed that variation in pathogen resilience can be explained by the differences in susceptible host dynamics, where faster replenishment of the susceptible pool corresponds to a more resilient host-pathogen system. Finally, we showed that pathogen resilience also determines the sensitivity to stochastic perturbations.

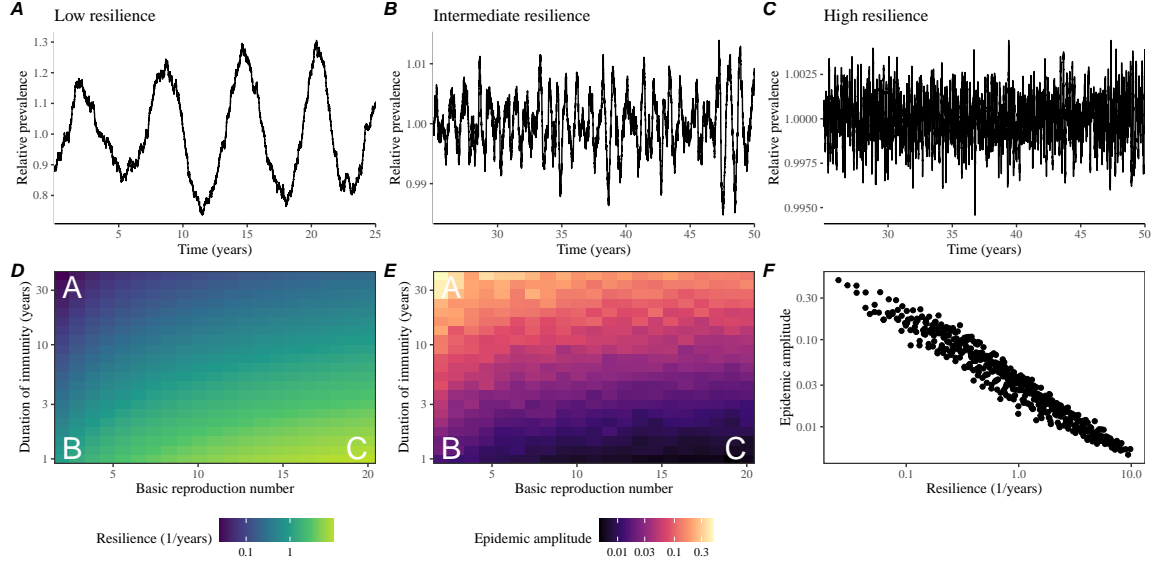


**Figure 6: Linking resilience of a host-pathogen system to its sensitivity to stochastic perturbations.** (A–C) Epidemic trajectories of a stochastic SIRS model across three different resilience values: low, intermediate, and high. The relative prevalence was calculated by dividing infection prevalence by its mean value. (D) Intrinsic resilience of a system as a function of the basic reproduction number  $\mathcal{R}_0$  and the duration of immunity. (E) Epidemic amplitude as a function of the basic reproduction number  $\mathcal{R}_0$  and the duration of immunity. The epidemic amplitude corresponds to  $(\max I - \min I)/(2\bar{I})$ , where  $\bar{I}$  represents the mean prevalence. Labels A–C in panels D and E correspond to scenarios shown in panels A–C. (F) The relationship between pathogen resilience and epidemic amplitude.

326 We analyzed case time series of common respiratory infections and norovirus  
 327 infections from Canada, Hong Kong, Korea, and the US to estimate their resilience.  
 328 Overall, we estimated the resilience of these pathogens to range from 0.4/year to  
 329 1.8/year, which is 3–14 times more resilient than prevaccination measles. These  
 330 resilience estimates indicate that common respiratory pathogens and norovirus likely  
 331 exhibit faster susceptible replenishment and are therefore more persistent, indicating  
 332 potential challenges in controlling these pathogens.

333 Based on our resilience estimates, we made phenomenological predictions about  
 334 when each pathogen will return to their endemic cycles. For the most part, we  
 335 accurately predicted which pathogens should have already returned before the end  
 336 of 2024. However, there were two main exceptions (i.e., norovirus in Hong Kong  
 337 and rhinovirus/enterovirus in the US), suggesting that these pathogens may be con-  
 338 verging to new endemic cycles or experiencing long-term transient behavior. These  
 339 changes may reflect changes in surveillance or actual shift in the dynamics, caused  
 340 by permanent changes in behavior or population-level immunity. While it may seem

341 unlikely that permanent changes in behavior would only affect a few pathogens and  
342 not others, we cannot rule out this possibility given differences in the observed mean  
343 age of infections and therefore the differences in age groups that primarily drive  
344 transmission [22, 23]. Differences in the mode of transmission between respiratory  
345 vs gastrointestinal pathogens may also contribute to the differences in responses to  
346 pandemic perturbations.

347 For almost half of the pathogens we considered, we predicted that their return  
348 to original epidemic patterns is imminent. We will need a few more years of data  
349 to test whether these pathogens will eventually return to their original dynamics or  
350 eventually converge to a different attractor. We also cannot rule out the possibility  
351 that some pathogens may exhibit long-term transient behaviors following pandemic  
352 perturbations. Overall, these observations echo earlier studies that highlighted the  
353 long-lasting impact of pandemic perturbations [8, 24, 25, 4].

354 We showed that susceptible host dynamics shape pathogen resilience, where faster  
355 replenishment of the susceptible population causes the pathogen to be more resilient.  
356 For simplicity, we focus on waning immunity and birth as the main drivers of the  
357 susceptible host dynamics but other mechanisms can also contribute to the replenish-  
358 ment of the susceptible population. In particular, pathogen evolution, especially the  
359 emergence of antigenically novel strains, can cause effective waning of immunity in  
360 the population; therefore, we hypothesize that the rate of antigenic evolution is likely  
361 a key feature of pathogen resilience. Future studies should explore the relationship  
362 between the rate of evolution and resilience for antigenically evolving pathogens.

363 Quantifying pathogen resilience also offers novel approaches to validating population-  
364 level epidemiological models. So far, most model validation in infectious disease ecol-  
365 ogy is based on the ability of a model to reproduce the observed epidemic dynamics  
366 and to predict future dynamics [26, 27, 28, 29, 30]. However, many models can  
367 perform similarly under these criteria. For example, two major RSV models have  
368 been proposed to explain biennial epidemic patterns: (1) a stage- and age-structured  
369 model that allows disease severity to vary with number of past infections and age of  
370 infection [28] and (2) a pathogen-interaction model that accounts for cross immunity  
371 between RSV and human metapneumovirus [27]. Since both models can accurately  
372 reproduce the observed epidemic patterns, standard criteria for model validation  
373 do not allow us to distinguish between these two models from population-level data  
374 alone. Instead, it would be possible to measure the empirical resilience of each model  
375 by simulating various perturbations and comparing the simulations to estimates of  
376 empirical resilience from data, using pandemic perturbations as a reference.

377 There are several limitations to our work. First, we did not extensively explore  
378 other approaches to reconstructing the attractor. Recent studies showed that more  
379 sophisticated approaches, such as using non-uniform embedding, can provide more  
380 robust reconstruction for noisy data [21]. In the context of causal inference, choices  
381 about embedding can have major impact on the resulting inference [31]. Our re-  
382 silience estimates are likely overly confident given a lack of uncertainties in attractor  
383 reconstruction as well as the simplicity of our statistical framework. Nonetheless,

as illustrated in our sensitivity analyses, inferences about pathogen resilience in our SIRS model appear to be robust to decisions about embedding lags and dimensions—this is because tracking the rate at which the system approaches the attractor is likely a much simpler problem than making inferences about causal directionality. Short pre-pandemic time series also limit our ability to accurately reconstruct the attractor and contribute to the crudeness of our resilience estimates; although this is less likely a problem for respiratory pathogens that are strongly annual, our attractor reconstruction may be inaccurate for those exhibiting multi-annual cycles, such as adenovirus in Hong Kong and Korea. Our framework also do not allow us to distinguish whether a system has settled to a new attractor or is experiencing long-term transient behavior. Uncertainties in pathogen dynamics due to changes in testing patterns further contribute to the crudeness of our resilience estimates. Despite these limitations, our qualitative prediction that common respiratory pathogens are more resilient than prevaccination measles is also likely to be robust, given how rapid many respiratory pathogens returned to their original cycles following pandemic perturbations.

Predicting the impact of anthropogenic changes on infectious disease dynamics is a fundamental aim of infectious disease research in a rapidly changing world. Our study illustrates that how a host-pathogen system responds to both small and large perturbations is largely predictable through the lens of ecological resilience. In particular, quantifying the resilience of a host-pathogen system offers a unique insight into questions about endemic pathogens' responses to pandemic perturbations, including whether some pathogens will exhibit long-lasting impact from the pandemic perturbation or not. More broadly, a detailed understanding of the determinants of pathogen resilience can provide deeper understanding of pathogen persistence.

## Materials and Methods

### Data

We gathered time series on respiratory infections from Canada, Hong Kong, Korea, and United States (US). As a reference, we also included time series data on norovirus infections when available. In contrast to respiratory pathogens, we hypothesized gastrointestinal viruses, such as norovirus, to be differently affected by pandemic perturbations.

Weekly time series of respiratory infection cases in Canada came from a publicly available website by the Respiratory Virus Detection Surveillance System, which collects data from select laboratories across Canada [32]. Weekly time series of respiratory infection cases in Hong Kong came from a publicly available website by the Centre for Health Protection, Department of Health [33, 34]. Weekly time series of acute respiratory infection cases in Korea came from a publicly available website by the Korea Disease Control and Prevention Agency [35]. Finally, weekly time series of respiratory infection cases in the US were obtained from the National Respiratory

424 and Enteric Virus Surveillance System. Time series on number of tests were also  
425 available in Canada, Hong Kong, and the US, but not in Korea.

## 426 Data processing

427 For all time series, we rounded every year to 52 weeks by taking the average number  
428 of cases and tests between the 52nd and 53rd week. We also rescale all time series to  
429 account for changes in testing patterns, which were then used for the actual analysis.

430 For Canada, an increase in testing was observed from 2013 to 2024 (Supplemen-  
431 tary Figure S17). To account for this increase, we calculated a 2 year moving average  
432 for the number of tests for each pathogen, which we used as a proxy for testing effort.  
433 Then, we divided the smoothed testing patterns by the smoothed value at the final  
434 week such that the testing effort has a maximum of 1. We then divided weekly cases  
435 by the testing effort to obtain a scaled case time series. A similar approach was used  
436 earlier for an analysis of RSV time series in the US to account for changes in testing  
437 patterns [28].

438 For Hong Kong, we applied the same scaling procedure to the time series as we  
439 did for Canada. In this case, we only adjusted for testing efforts up to the end of 2019  
440 because there was a major reduction in testing for common respiratory pathogens  
441 between 2020 and 2023 (Supplementary Figure S18).

442 For Korea, while we did not have information on testing, the reported number  
443 of respiratory infections consistently increased from 2013 to the end of 2019, which  
444 we interpreted as changes in testing patterns (Supplementary Figure S19). Since  
445 we did not have testing numbers, we used the weekly sum of all acute respiratory  
446 viral infection cases as a proxy for testing, which were further smoothed with moving  
447 averaged and scaled to have a maximum of 1. For Korea, we also only adjusted for  
448 testing efforts up to the end of 2019.

449 In the US, there has been a large increase in testing against some respiratory  
450 pathogens, especially RSV, which could not be corrected by simple scaling (Supple-  
451 mentary Figure S20). Instead, we derived an incidence proxy by multiplying the  
452 test positivity with influenza-like illness positivity, which was taken from <https://gis.cdc.gov/grasp/fluview/fluportaldashboard.html>. This method of es-  
453 timating an incidence proxy has been recently applied in the analysis of seasonal  
454 coronaviruses [7] and *Mycoplasma pneumoniae* infections [4]. Detailed assumptions  
455 and justifications are provided in [36].

## 457 Data summary

458 To make qualitative comparisons between pre- and post-perturbation dynamics of  
459 respiratory pathogen circulation patterns, we calculate the mean seasonal patterns  
460 using time series of either rescaled cases or incidence proxy estimates before 2020. We  
461 do so by taking the mean value in each week across all years before 2020. Confidence  
462 intervals around the means are calculated using a simple t test.

## 463 Estimating pathogen resilience

464 In order to measure pathogen resilience from surveillance data, we first reconstructed  
 465 the empirical pre-pandemic attractor of the system using Takens' embedding theorem  
 466 [17]. Specifically, for a given pathogen, we took the pre-pandemic (before 2020) case  
 467 time series  $C(t)$  and reconstructed the attractor using delayed embedding with a  
 468 uniform delay of  $\tau$  and dimension  $M$ :

$$X_{\tau,m}(t) = \langle \log(C(t) + 1), \log(C(t - \tau) + 1), \dots, \log(C(t - (M-1)\tau) + 1) \rangle. \quad (2)$$

469 Here, the delay  $\tau$  was determined by calculating the autocorrelation of the logged  
 470 pre-pandemic time series and asking when the autocorrelation crosses 0 for the first  
 471 time [21]; a typical delay for an annual outbreak is around 13 weeks.

472 Then, for a given delay  $\tau$ , we determined the embedding dimension  $M$  using the  
 473 false nearest neighbors approach [20, 21]. To do so, we started with an embedding  
 474 dimension  $e$  and constructed a set of points  $A_{\tau,e} = \{X_{\tau,e}(t) | t < 2020\}$ . Then, for  
 475 each point  $X_{\tau,e}(t)$ , we determined the nearest neighbor from the set  $A_{\tau,e}$ , which we  
 476 denote  $X_{\tau,e}(t_{nn})$  for  $t \neq t_{nn}$ . Then, if the distance between these two points in the  
 477  $e+1$  dimension,  $D_{\tau,e+1}(t) = \|X_{\tau,e+1}(t_{nn}) - X_{\tau,e+1}(t)\|_2$ , is larger than their distance  
 478 in the  $e$  dimension,  $D_{\tau,e}(t) = \|X_{\tau,e}(t_{nn}) - X_{\tau,e}(t)\|_2$ , these two points are deemed to  
 479 be false nearest neighbors; specifically, we used a threshold  $R$  for the ratio between  
 480 two distances  $D_{\tau,e+1}(t)/D_{\tau,e}(t)$  to determine false nearest neighbors. For the main  
 481 analysis, we used  $R = 10$ , which was chosen from a sensitivity analysis against  
 482 simulated data (Supplementary Text). Once we determined the embedding lag  $\tau$   
 483 and dimension  $M$ , we apply the embedding to the entire time series and calculate  
 484 the nearest neighbor distance against the attractor  $A_{\tau,M}$  to obtain a time series of  
 485 distance from the attractor  $D_{\tau,M}(t)$ .

486 From a time series of distances from the attractor, we estimated pathogen re-  
 487 silience by fitting a linear regression to an appropriate window. To automatically se-  
 488 lect the fitting window, we began by smoothing the distance time series using locally  
 489 estimated scatterplot smoothing (LOESS) to obtain  $\hat{D}_{\tau,M}(t)$ , where the smoothing  
 490 is performed on a log scale and exponentiated afterwards. Then, we determined  
 491 threshold values ( $T_{\text{start}}$  and  $T_{\text{end}}$ ) for the smoothed distances and choose the fitting  
 492 window based on when  $\hat{D}_{\tau,M}(t)$  crosses these threshold values for the first time.  
 493 These thresholds were determined by first calculating the maximum distance,

$$\max \hat{D} = \max \hat{D}_{\tau,M}(t), \quad (3)$$

494 and the mean pre-pandemic distance,

$$\hat{D}_{\text{mean}} = \frac{1}{N_{t<2020}} \sum_{t<2020} \hat{D}_{\tau,M}(t), \quad (4)$$

495 as a reference, and then dividing their ratios into  $K$  equal bins,

$$T_{\text{start}} = \hat{D}_{\text{mean}} \times \left( \frac{\max \hat{D}}{\hat{D}_{\text{mean}}} \right)^{(K-a)/K}, \quad (5)$$

$$T_{\text{end}} = \hat{D}_{\text{mean}} \times \left( \frac{\max \hat{D}}{\hat{D}_{\text{mean}}} \right)^{a/K}, \quad (6)$$

496 where  $a$  represents the truncation threshold. This allows us to discard the initial  
 497 period during which the distance increases (from the introduction of intervention  
 498 measures) and the final period during which the distance plateaus (as the system  
 499 reaches an attractor). The fitting window is determined based on when the smoothed  
 500 distance  $\hat{D}_{\tau,M}(t)$  crosses these threshold values for the first time; then, we fit a  
 501 linear regression to logged (unsmoothed) distances  $\log D_{\tau,M}(t)$  using that window.  
 502 Alongside the threshold  $R$  for the false nearest neighbors approach, we tested optimal  
 503 choices for  $K$  and  $a$  values using simulations (Supplementary Text). We used  $K = 19$   
 504 and  $a = 2$  throughout the paper based on the simulation results.

## 505 Mathematical modeling

506 Throughout the paper, we use a series of mathematical models to illustrate the  
 507 concept of pathogen resilience and to understand the determinants of pathogen re-  
 508 silience. In general, the intrinsic resilience of a given system is given by the largest  
 509 real part of the eigenvalues of the linearized system at endemic equilibrium. Here, we  
 510 focus on the SIRS model with demography (birth and death) and present the details  
 511 of other models in Supplementary Text. The SIRS (Susceptible-Infected-Recovered-  
 512 Susceptible) model is the simplest model that allows for waning of immunity, where  
 513 recovered (immune) individuals are assumed to become fully susceptible after an  
 514 average of  $1/\delta$  time period. The dynamics of the SIRS model is described by the  
 515 following set of differential equations:

$$\frac{dS}{dt} = \mu - \beta(t)SI - \mu S + \delta R \quad (7)$$

$$\frac{dI}{dt} = \beta(t)SI - (\gamma + \mu)I \quad (8)$$

$$\frac{dR}{dt} = \gamma I - (\delta + \mu)R \quad (9)$$

(10)

516 where  $\mu$  represents the birth and death rates,  $\beta(t)$  represents the time-varying trans-  
 517 mission rate, and  $\gamma$  represents the recovery rate. The basic reproduction number  
 518  $\mathcal{R}_0(t) = \beta(t)/(\gamma + \mu)$  is defined as the average number of secondary infections that  
 519 a single infected individual would cause in a fully susceptible population at time  $t$   
 520 and measures the intrinsic transmissibility of a pathogen.

521 When we introduced the idea of pathogen resilience (Figure 2), we imposed sinu-  
 522 soidal changes to the transmission rate to account for seasonal transmission,

$$\beta(t) = b_1(1 + \theta \cos(2\pi(t - \phi)))\alpha(t), \quad (11)$$

523 where  $b_1$  represents the baseline transmission rate,  $\theta$  represents the seasonal amplitude,  
 524 and  $\phi$  represents the seasonal offset term. Here, we also introduced an extra  
 525 multiplicative term  $\alpha(t)$  to account for the impact of pandemic perturbations, where  
 526  $\alpha(t) < 1$  indicates transmission reduction. Figure 2A and 2B were generated assuming  
 527  $b_1 = 3 \times (365/7 + 1/50)/\text{years}$ ,  $\theta = 0.2$ ,  $\phi = 0$ ,  $\mu = 1/50/\text{years}$ ,  $\gamma = 365/7/\text{years}$ ,  
 528 and  $\delta = 1/2/\text{years}$ . In Figure 2A, we imposed a 50% transmission reduction for 6  
 529 months from 2020:

$$\alpha(t) = \begin{cases} 0.5 & 2020 \leq t < 2020.5 \\ 1 & \text{otherwise} \end{cases} \quad (12)$$

530 In Figure 2B, we imposed a 50% transmission reduction for 6 months from 2020 and  
 531 a permanent 10% reduction onward:

$$\alpha(t) = \begin{cases} 1 & t < 2020 \\ 0.5 & 2020 \leq t < 2020.5 \\ 0.9 & 2020.5 \leq t \end{cases} \quad (13)$$

532 In both scenarios, we simulated the SIRS model from the same initial conditions  
 533 ( $S(0) = 1/\mathcal{R}_0$ ,  $I(0) = 1 \times 10^{-6}$ , and  $R(0) = 1 - S(0) - I(0)$ ) from 1900 until 2030.

534 To measure the empirical resilience of the SIRS model (Figure 2C and 2F), we  
 535 computed the normalized distance between post-intervention susceptible and logged  
 536 infected proportions and their corresponding unperturbed values at the same time:

$$\sqrt{\left(\frac{S(t) - S_{\text{unperturbed}}(t)}{\sigma_S}\right)^2 + \left(\frac{\log I(t) - \log I_{\text{unperturbed}}(t)}{\sigma_{\log I}}\right)^2}, \quad (14)$$

537 where  $\sigma_S$  and  $\sigma_{\log I}$  represent the standard deviation in the unperturbed susceptible  
 538 and logged infected proportions. The unperturbed values were obtained by simulating  
 539 the same SIRS model without pandemic perturbations ( $\alpha = 1$ ). We normalized  
 540 the differences in susceptible and logged infected proportions to allow both quantities  
 541 to equally contribute to the changes in distance from the attractor. We used logged  
 542 prevalence, instead of absolute prevalence, in order to capture epidemic dynamics  
 543 in deep troughs during the intervention period. In Supplementary Materials, we  
 544 also compared how the degree of seasonal transmission affects empirical resilience  
 545 by varying  $\theta$  from 0 to 0.4; when we assumed no seasonality ( $\theta = 0$ ), we did not  
 546 normalize the distance because the standard deviation of pre-intervention dynamics  
 547 are zero.

548 We used the SIRS model to understand how underlying epidemiological parameters  
 549 affect pathogen resilience and determine the relationship to underlying sus-  
 550 ceptible host dynamics. For the simple SIRS model without seasonal transmission  
 551 ( $\theta = 0$ ), the intrinsic resilience equals

$$-\frac{\text{Re}(\lambda)}{2} = \frac{\delta + \beta I^* + \mu}{2}. \quad (15)$$

552 Here,  $I^*$  represents the prevalence at endemic equilibrium:

$$I^* = \frac{(\delta + \mu)(\beta - (\gamma + \mu))}{\beta(\delta + \gamma + \mu)}. \quad (16)$$

553 The susceptible replenishment rate is given by

$$S_{\text{replenish}} = \frac{\mu + \delta R}{S^*}, \quad (17)$$

554 where  $S^* = 1/\mathcal{R}_0$  represents the equilibrium proportion of susceptible individuals.  
555 We varied the basic reproduction number  $\mathcal{R}_0$  between 1.1 to 6 and the average  
556 duration of immunity  $1/\delta$  between 2 to 4 years, and computed these two quantities.  
557 In doing so, we fixed all other parameters:  $\mu = 1/80/\text{years}$  and  $\gamma = 365/7/\text{years}$ .  
558 When infection provides a life-long immunity ( $\delta = 0$ ), the intrinsic resilience is  
559 inversely proportional to the susceptible replenishment rate:

$$-\frac{\text{Re}(\lambda)}{2} = \frac{\mu}{2S^*} = \frac{S_{\text{replenish}}}{2}. \quad (18)$$

560 Finally, we used a seasonally unforced stochastic SIRS model without demog-  
561 raphy to understand how pathogen resilience affects sensitivity of the system to  
562 demographic stochasticity (see Supplementary Text for the details of the stochas-  
563 tic SIRS model). By varying the basic reproduction number  $\mathcal{R}_0$  between 2 to 20  
564 and the average duration of immunity  $1/\delta$  between 1 to 40 years, we ran the SIRS  
565 model for 100 years and computed the epidemic amplitude, which we defined as  
566  $(\max I - \min I)/(2\bar{I})$ . Each simulation began from the equilibrium, and we trun-  
567 cated the initial 25 years before computing the epidemic amplitude. In doing so,  
568 we assumed  $\gamma = 365/7/\text{years}$  and fixed the population size to 1 billion to prevent  
569 any fadeouts. We also considered a seasonally forced stochastic SIRS model without  
570 demography, assuming an amplitude of seasonal forcing of 0.04; in this case, we com-  
571 puted the relative epidemic amplitude by comparing the deterministic and stochastic  
572 trajectories (Supplementary Materials).

## 573 Data availability

574 All data and code are stored in a publicly available GitHub repository (<https://github.com/cobeylab/return-time>).

## 576 Funding

577 S.W.P. is a Peter and Carmen Lucia Buck Foundation Awardee of the Life Sciences  
578 Research Foundation. S.C. was supported by Federal funds from the National Insti-  
579 tute of Allergy and Infectious Diseases, National Institutes of Health, Department of  
580 Health and Human Services under CEIRR contract 75N93021C00015. The content is  
581 solely the responsibility of the authors and does not necessarily represent the official  
582 views of the NIAID or the National Institutes of Health.

583 **Supplementary Text**

584 **Resilience of a stage-structured system.**

585 In Figure 2G–I, we used a more realistic, stage-structured model to illustrate how  
 586 transient phenomena can cause the system to slow down. Specifically, we used the  
 587 stage-structured RSV model proposed by [28], which assumes that subsequent rein-  
 588 fections cause an individual to become less susceptible and transmissible than previ-  
 589 ous infections. The model dynamics can be described as follows:

$$\frac{dM}{dt} = \mu - (\omega + \mu)M \quad (S1)$$

$$\frac{dS_0}{dt} = \omega M - (\lambda(t) + \mu)S_0 \quad (S2)$$

$$\frac{dI_1}{dt} = \lambda(t)S_0 - (\gamma_1 + \mu)I_1 \quad (S3)$$

$$\frac{dS_1}{dt} = \gamma_1 I_1 - (\sigma_1 \lambda(t) + \mu)S_1 \quad (S4)$$

$$\frac{dI_2}{dt} = \sigma_1 \lambda(t)S_1 - (\gamma_2 + \mu)I_2 \quad (S5)$$

$$\frac{dS_2}{dt} = \gamma_2 I_2 - (\sigma_2 \lambda(t) + \mu)S_2 \quad (S6)$$

$$\frac{dI_3}{dt} = \sigma_2 \lambda(t)S_2 - (\gamma_3 + \mu)I_3 \quad (S7)$$

$$\frac{dS_3}{dt} = \gamma_3 I_3 - (\sigma_3 \lambda(t) + \mu)S_3 + \gamma_4 I_4 \quad (S8)$$

$$\frac{dI_4}{dt} = \sigma_3 \lambda(t)S_3 - (\gamma_4 + \mu)I_4 \quad (S9)$$

(S10)

590 where  $M$  represents the proportion of individuals who are maternally immune;  $S_i$   
 591 represents the proportion of individuals who are susceptible after  $i$  prior infections;  $I_i$   
 592 represents the proportion of individuals who are currently (re)-infected with their  $i$ -th  
 593 infection;  $\mu$  represents the birth and death rates;  $1/\omega$  represents the mean duration  
 594 of maternal immunity;  $1/\gamma_i$  represents the mean duration of infection;  $\lambda(t)$  represents  
 595 the force of infection; and  $\sigma_i$  represents the reduction in susceptibility for the  $i$ -th  
 596 reinfection. The force of infection is modeled using a sinusoidal function:

$$\beta(t) = b_1(1 + \theta \cos(2\pi(t - \phi)))\alpha(t) \quad (S11)$$

$$\lambda(t) = \beta(I_1 + \rho_1 I_2 + \rho_2(I_3 + I_4)), \quad (S12)$$

597 where  $b_1$  represents the baseline transmission rate;  $\theta$  represents the seasonal ampli-  
 598 tude;  $\phi$  represents the seasonal offset term;  $\alpha(t)$  represents the intervention effect;  
 599 and  $\rho_i$  represents the impact of immunity on transmission reduction. We used the

following parameters to simulate the impact of interventions on epidemic dynamics [28]:  $b_1 = 9 \times (365/10 + 1/80)/\text{years}$ ,  $\theta = 0.2$ ,  $\phi = -0.1$ ,  $\omega = 365/112/\text{years}$ ,  $\gamma_1 = 365/10/\text{years}$ ,  $\gamma_2 = 365/7/\text{years}$ ,  $\gamma_3 = 365/5/\text{years}$ ,  $\sigma_1 = 0.76$ ,  $\sigma_2 = 0.6$ ,  $\sigma_3 = 0.4$ ,  $\rho_1 = 0.75$ ,  $\rho_2 = 0.51$ , and  $\mu = 1/80/\text{years}$ . We assumed a 50% transmission reduction for 6 months from 2020:

$$\alpha(t) = \begin{cases} 0.5 & 2020 \leq t < 2020.5 \\ 1 & \text{otherwise} \end{cases} \quad (\text{S13})$$

The model was simulated from 1900 to 2030 using the following initial conditions:  $M = 0$ ,  $S_0 = 1/\mathcal{R}_0 - I_1$ ,  $I_1 = 1 \times 10^{-6}$ ,  $S_1 = 1 - 1/\mathcal{R}_0$ ,  $I_2 = 0$ ,  $S_2 = 0$ ,  $I_3 = 0$ ,  $S_3 = 0$ , and  $I_4 = 0$ . For the phase plane analysis (Figure 2H) and distance analysis (Figure 2I), we relied on the average susceptibility,

$$\bar{S} = S_0 + \sigma_1 S_1 + \sigma_2 S_2 + \sigma_3 S_3, \quad (\text{S14})$$

and total prevalence,

$$I_{\text{total}} = I_1 + I_2 + I_3 + I_4. \quad (\text{S15})$$

These quantities were used to compute the normalized distance from the attractor, as described in the main text.

## Resilience of a multistrain system.

We used a simple two-strain model to show that a multistrain host-pathogen system that is coupled through cross immunity can be described by a single resilience value. The model dynamics can be described as follows [27]:

$$\frac{dS}{dt} = \mu - \mu S - (\lambda_1 + \lambda_2)S + \rho_1 R_1 + \rho_2 R_2 \quad (\text{S16})$$

$$\frac{dI_1}{dt} = \lambda_1 S - (\gamma_1 + \mu)I_1 \quad (\text{S17})$$

$$\frac{dI_2}{dt} = \lambda_2 S - (\gamma_2 + \mu)I_2 \quad (\text{S18})$$

$$\frac{dR_1}{dt} = \gamma_1 I_1 - \lambda_2 \epsilon_{21} R_1 - \rho_1 R_1 + \rho_2 R - \mu R_1 \quad (\text{S19})$$

$$\frac{dR_2}{dt} = \gamma_2 I_2 - \lambda_1 \epsilon_{12} R_2 - \rho_2 R_2 + \rho_1 R - \mu R_2 \quad (\text{S20})$$

$$\frac{dJ_1}{dt} = \lambda_1 \epsilon_{12} R_2 - (\gamma_1 + \mu)J_1 \quad (\text{S21})$$

$$\frac{dJ_2}{dt} = \lambda_2 \epsilon_{21} R_1 - (\gamma_2 + \mu)J_2 \quad (\text{S22})$$

$$\frac{dR}{dt} = \gamma_1 J_1 + \gamma_2 J_2 - \rho_1 R - \rho_2 R - \mu R \quad (\text{S23})$$

where  $S$  represents the proportion of individuals who are fully susceptible to infections by both strains;  $I_1$  represents the proportion of individuals who are infected with strain 1 without prior immunity;  $I_2$  represents the proportion of individuals who are infected with strain 2 without prior immunity;  $R_1$  represents the proportion of individuals who are fully immune against strain 1 and partially susceptible to reinfection by strain 2;  $R_2$  represents the proportion of individuals who are fully immune against strain 2 and partially susceptible to reinfection by strain 1;  $J_1$  represents the proportion of individuals who are infected with strain 1 with prior immunity against strain 2;  $J_2$  represents the proportion of individuals who are infected with strain 2 with prior immunity against strain 1;  $R$  represents the proportion of individuals who are immune to infections from both strains;  $\mu$  represents the birth/death rate;  $\lambda_1$  and  $\lambda_2$  represent the force of infection from strains 1 and 2, respectively;  $\rho_1$  and  $\rho_2$  represent the waning immunity rate;  $\gamma_1$  and  $\gamma_2$  represent the recovery rate;  $\epsilon_{12}$  and  $\epsilon_{21}$  represent the susceptibility to reinfection with strains 2 and 1, respectively, given prior immunity from infection with strains 1 and 2, respectively. The force of infection is modeled as follows:

$$\beta_1 = b_1(1 + \theta_1 \sin(2\pi(t - \phi_1)))\alpha(t) \quad (\text{S24})$$

$$\beta_2 = b_2(1 + \theta_2 \sin(2\pi(t - \phi_2)))\alpha(t) \quad (\text{S25})$$

$$\lambda_1 = \beta_1(I_1 + J_1) \quad (\text{S26})$$

$$\lambda_2 = \beta_2(I_2 + J_2) \quad (\text{S27})$$

In Supplementary Figures S2–S4, we assumed the following parameters:  $b_1 = 2 \times 52/\text{years}$ ,  $b_2 = 4 \times 52/\text{years}$ ,  $\phi_1 = \phi_2 = 0$ ,  $\epsilon_{12} = 0.9$ ,  $\epsilon_{21} = 0.5$ ,  $\gamma_1 = \gamma_2 = 52/\text{years}$ ,  $\rho_1 = \rho_2 = 1/\text{years}$ , and  $\mu = 1/70/\text{years}$ . For all simulations, we assumed a 50% transmission reduction for 6 months from 2020:

$$\alpha(t) = \begin{cases} 0.5 & 2020 \leq t < 2020.5 \\ 1 & \text{otherwise} \end{cases} \quad (\text{S28})$$

The seasonal amplitude  $\theta$  is varied from 0 to 0.4. All simulations were ran from 1900 to 2030 with following initial conditions:  $S(0) = 1 - 2 \times 10^{-6}$ ,  $I_1(0) = 1 \times 10^{-6}$ ,  $I_2(0) = 1 \times 10^{-6}$ ,  $R_1(0) = 0$ ,  $R_2(0) = 0$ ,  $J_1(0) = 0$ ,  $J_2(0) = 0$ , and  $R(0) = 0$ .

We considered three scenarios for measuring pathogen resilience: (1) we only have information about strain 1, (2) we only have information about strain 2, and (3) we are unable to distinguish between strains. In the first two scenarios (see panels A–C for strain 1 and panels D–F for strain 2), we considered the dynamics of average susceptibility for each strain and total prevalence:

$$\bar{S}_1 = S + \epsilon_{12}R_2 \quad (\text{S29})$$

$$\hat{I}_1 = I_1 + J_1 \quad (\text{S30})$$

$$\bar{S}_2 = S + \epsilon_{21}R_1 \quad (\text{S31})$$

$$\hat{I}_2 = I_2 + J_2 \quad (\text{S32})$$

644 In the third scenario (panels G–I), we considered the dynamics of total susceptible  
645 and infected populations:

$$\hat{S} = S + R_2 + R_1 \quad (\text{S33})$$

$$\hat{I} = I_1 + J_1 + I_2 + J_2 \quad (\text{S34})$$

646 These quantities were used to compute the normalized distance from the attractor,  
647 as described in the main text.

## 648 Estimating intrinsic resilience using a mechanistic model

649 We tested whether we can reliably estimate the intrinsic resilience of a system by fit-  
650 ting a mechanistic model. Specifically, we simulated case time series from stochastic  
651 SIRS and two-strain models and fitted a simple, deterministic SIRS model using a  
652 Bayesian framework.

653 We simulated the models in discrete time with a daily time step ( $\Delta t = 1$ ),  
654 incorporating demographic stochasticity:

$$\beta(t) = \mathcal{R}_0 \left( 1 + \theta \cos \left( \frac{2\pi t}{364} \right) \right) \alpha(t)(1 - \exp(-\gamma)) \quad (\text{S35})$$

$$\text{FOI}(t) = \beta(t)I(t - \Delta t)/N \quad (\text{S36})$$

$$B(t) \sim \text{Poisson}(\mu N) \quad (\text{S37})$$

$$\Delta S(t) \sim \text{Binom}(S(t - \Delta t), 1 - \exp(-(\text{FOI}(t) + \mu)\Delta t)) \quad (\text{S38})$$

$$N_{SI}(t) \sim \text{Binom}\left(\Delta S(t), \frac{\text{FOI}(t)}{\text{FOI}(t) + \mu}\right) \quad (\text{S39})$$

$$\Delta I(t) \sim \text{Binom}(I(t - \Delta t), 1 - \exp(-(\gamma + \mu)\Delta t)) \quad (\text{S40})$$

$$N_{IR}(t) \sim \text{Binom}\left(\Delta I(t), \frac{\gamma}{\gamma + \mu}\right) \quad (\text{S41})$$

$$\Delta R(t) \sim \text{Binom}(R(t - \Delta t), 1 - \exp(-(\delta + \mu)\Delta t)) \quad (\text{S42})$$

$$N_{RS}(t) \sim \text{Binom}\left(\Delta R(t), \frac{\delta}{\delta + \mu}\right) \quad (\text{S43})$$

$$S(t) = S(t - \Delta t) + N_{RS}(t) + B(t) - \Delta S(t) \quad (\text{S44})$$

$$I(t) = I(t - \Delta t) + N_{SI}(t) - \Delta I(t) \quad (\text{S45})$$

$$R(t) = R(t - \Delta t) + N_{IR}(t) - \Delta R(t) \quad (\text{S46})$$

655 where FOI represents the force of infection;  $N_{ij}$  represents the number of individuals  
656 moving from compartment  $i$  to  $j$  on a given day; and  $B(t)$  represents the number  
657 of new births. All other parameters definitions can be found in the description of  
658 the deterministic version of the model. We simulated the model on a daily scale—  
659 assuming 364 days in a year so that it can be evenly grouped into 52 weeks—with  
660 the following parameters:  $\mathcal{R}_0 = 3$ ,  $\theta = 0.1$ ,  $\gamma = 1/7/\text{days}$ ,  $\delta = 1/(364 \times 2)/\text{days}$ ,

<sup>661</sup>  $\mu = 1/(364 \times 50)/\text{days}$ , and  $N = 1 \times 10^8$ . The model was simulated from 1900 to  
<sup>662</sup> 2030 assuming  $S(0) = N/3$ ,  $I(0) = 100$ , and  $R(0) = N - S(0) - I(0)$ . The observed  
<sup>663</sup> incidence from the model was then simulated as follows:

$$C(t) = \text{Beta-Binom}(N_{SI}(t), \rho, k), \quad (\text{S47})$$

<sup>664</sup> where  $\rho$  represents the reporting probability and  $k$  represents the overdispersion  
<sup>665</sup> parameter of beta-binomial distribution. Here, we used the beta-binomial distribu-  
<sup>666</sup> tion to account for overdispersion in reporting. We assumed  $\rho = 0.002$  (i.e., 0.2%  
<sup>667</sup> probability) and  $k = 1000$ .

<sup>668</sup> We used an analogous approach for the two-strain model:

$$\beta_1(t) = b_1 \left( 1 + \theta_1 \cos \left( \frac{2\pi(t - \phi_1)}{364} \right) \right) \alpha(t) \quad (\text{S48})$$

$$\beta_2(t) = b_2 \left( 1 + \theta_2 \cos \left( \frac{2\pi(t - \phi_2)}{364} \right) \right) \alpha(t) \quad (\text{S49})$$

$$\text{FOI}_1(t) = \beta_1(t)(I_1(t - \Delta t) + J_1(t - \Delta t))/N \quad (\text{S50})$$

$$\text{FOI}_2(t) = \beta_2(t)(I_2(t - \Delta t) + J_2(t - \Delta t))/N \quad (\text{S51})$$

$$B(t) \sim \text{Poisson}(\mu N) \quad (\text{S52})$$

$$\Delta S(t) \sim \text{Binom}(S(t - \Delta t), 1 - \exp(-(\text{FOI}_1(t) + \text{FOI}_2(t) + \mu)\Delta t)) \quad (\text{S53})$$

$$N_{SI_1}(t) \sim \text{Binom}\left(\Delta S(t), \frac{\text{FOI}_1(t)}{\text{FOI}_1(t) + \text{FOI}_2(t) + \mu}\right) \quad (\text{S54})$$

$$N_{SI_2}(t) \sim \text{Binom}\left(\Delta S(t), \frac{\text{FOI}_2(t)}{\text{FOI}_1(t) + \text{FOI}_2(t) + \mu}\right) \quad (\text{S55})$$

$$\Delta I_1(t) \sim \text{Binom}(I_1(t - \Delta t), 1 - \exp(-(\gamma_1 + \mu)\Delta t)) \quad (\text{S56})$$

$$N_{I_1 R_1}(t) \sim \text{Binom}\left(\Delta I_1(t), \frac{\gamma_1}{\gamma_1 + \mu}\right) \quad (\text{S57})$$

$$\Delta I_2(t) \sim \text{Binom}(I_2(t - \Delta t), 1 - \exp(-(\gamma_2 + \mu)\Delta t)) \quad (\text{S58})$$

$$N_{I_2 R_2}(t) \sim \text{Binom}\left(\Delta I_2(t), \frac{\gamma_2}{\gamma_2 + \mu}\right) \quad (\text{S59})$$

$$\Delta R_1(t) \sim \text{Binom}(R_1(t - \Delta t), 1 - \exp(-(\epsilon_{21}\text{FOI}_2(t) + \rho_1 + \mu)\Delta t)) \quad (\text{S60})$$

$$N_{R_1 S}(t) \sim \text{Binom}\left(\Delta R_1(t), \frac{\rho_1}{\epsilon_{21}\text{FOI}_2(t) + \rho_1 + \mu}\right) \quad (\text{S61})$$

$$N_{R_1 J_2}(t) \sim \text{Binom}\left(\Delta R_1(t), \frac{\epsilon_{21}\text{FOI}_2(t)}{\epsilon_{21}\text{FOI}_2(t) + \rho_1 + \mu}\right) \quad (\text{S62})$$

$$\Delta R_2(t) \sim \text{Binom}(R_2(t - \Delta t), 1 - \exp(-(\epsilon_{12}\text{FOI}_1(t) + \rho_2 + \mu)\Delta t)) \quad (\text{S63})$$

$$N_{R_2 S}(t) \sim \text{Binom}\left(\Delta R_2(t), \frac{\rho_2}{\epsilon_{12}\text{FOI}_1(t) + \rho_2 + \mu}\right) \quad (\text{S64})$$

$$N_{R_2 J_1}(t) \sim \text{Binom}\left(\Delta R_2(t), \frac{\epsilon_{12}\text{FOI}_1(t)}{\epsilon_{12}\text{FOI}_1(t) + \rho_2 + \mu}\right) \quad (\text{S65})$$

$$\Delta J_1(t) \sim \text{Binom}(J_1(t - \Delta t), 1 - \exp(-(\gamma_1 + \mu)\Delta t)) \quad (\text{S66})$$

$$N_{J_1R}(t) \sim \text{Binom}\left(\Delta J_1(t), \frac{\gamma_1}{\gamma_1 + \mu}\right) \quad (\text{S67})$$

$$\Delta J_2(t) \sim \text{Binom}(J_2(t - \Delta t), 1 - \exp(-(\gamma_2 + \mu)\Delta t)) \quad (\text{S68})$$

$$N_{J_2R}(t) \sim \text{Binom}\left(\Delta J_2(t), \frac{\gamma_2}{\gamma_2 + \mu}\right) \quad (\text{S69})$$

$$\Delta R(t) \sim \text{Binom}(R(t - \Delta t), 1 - \exp(-(\rho_1 + \rho_2 + \mu)\Delta t)) \quad (\text{S70})$$

$$N_{RR_1}(t) \sim \text{Binom}\left(\Delta R(t), \frac{\rho_1}{\rho_1 + \rho_2 + \mu}\right) \quad (\text{S71})$$

$$N_{RR_2}(t) \sim \text{Binom}\left(\Delta R(t), \frac{\rho_2}{\rho_1 + \rho_2 + \mu}\right) \quad (\text{S72})$$

$$S(t) = S(t - \Delta t) - \Delta S(t) + B(t) + N_{R_1S}(t) + N_{R_2S}(t) \quad (\text{S73})$$

$$I_1(t) = I_1(t - \Delta t) - \Delta I_1(t) + N_{SI_1}(t) \quad (\text{S74})$$

$$I_2(t) = I_2(t - \Delta t) - \Delta I_2(t) + N_{SI_2}(t) \quad (\text{S75})$$

$$R_1(t) = R_1(t - \Delta t) - \Delta R_1(t) + N_{I_1R_1}(t) + N_{RR_1}(t) \quad (\text{S76})$$

$$R_2(t) = R_2(t - \Delta t) - \Delta R_2(t) + N_{I_2R_2}(t) + N_{RR_2}(t) \quad (\text{S77})$$

$$J_1(t) = J_1(t - \Delta t) - \Delta J_1(t) + N_{R_2J_1}(t) \quad (\text{S78})$$

$$J_2(t) = J_2(t - \Delta t) - \Delta J_2(t) + N_{R_1J_2}(t) \quad (\text{S79})$$

$$R(t) = R(t - \Delta t) - \Delta R(t) + N_{J_1R}(t) + N_{J_2R}(t) \quad (\text{S80})$$

669 We simulated the model on a daily scale with previously estimated parameters for the  
 670 RSV-HMPV interaction [27]:  $b_1 = 1.7/\text{weeks}$ ,  $b_2 = 1.95/\text{weeks}$ ,  $\theta_1 = 0.4$ ,  $\theta_2 = 0.3$ ,  
 671  $\phi_1 = 0.005 \times 7/364$ ,  $\phi_2 = 4.99 \times 7/364$ ,  $\epsilon_{12} = 0.92$ ,  $\epsilon_{21} = 0.45$ ,  $\gamma_1 = 1/10/\text{days}$ ,  
 672  $\gamma_2 = 1/10/\text{days}$ ,  $\rho_1 = 1/364/\text{days}$ ,  $\rho_2 = 1/364/\text{days}$ ,  $\mu = 1/(70 \times 364)/\text{days}$ , and  
 673  $N = 1 \times 10^8$ . The model was simulated from 1900 to 2030 assuming  $S(0) = N - 200$ ,  
 674  $I_1(0) = 100$ ,  $I_2(0) = 100$ ,  $R_1(0) = 0$ ,  $R_2(0) = 0$ ,  $J_1(0) = 0$ ,  $J_2(0) = 0$ , and  $R(0) = 0$ .  
 675 The observed incidence for each strain is then simulated as follows:

$$C_1(t) = \text{Beta-Binom}(N_{SI_1}(t) + N_{R_2J_1}, \rho, k), \quad (\text{S81})$$

$$C_2(t) = \text{Beta-Binom}(N_{SI_2}(t) + N_{R_1J_2}, \rho, k), \quad (\text{S82})$$

676 where  $\rho$  represents the reporting probability and  $k$  represents the overdispersion pa-  
 677 rameter of beta-binomial distribution. We assumed  $\rho = 0.002$  (i.e., 0.2% probability)  
 678 and  $k = 500$ . We also considered the total incidence:  $C_{\text{total}}(t) = C_1(t) + C_2(t)$ .

679 For both models, we considered a more realistically shaped pandemic pertur-  
 680 bation  $\alpha(t)$  to challenge our ability to estimate the intervention effects. Thus, we  
 681 assumed a 40% transmission reduction for 3 months from March 2020, followed by a  
 682 10% transmission reduction for 6 months, 20% transmission reduction for 3 months,

683 and a final return to normal levels:

$$\alpha(t) = \begin{cases} 1 & t < 2020.25 \\ 0.6 & 2020.25 \leq t < 2020.5 \\ 0.9 & 2020.5 \leq t < 2021 \\ 0.8 & 2021 \leq t < 2021.25 \\ 1 & 2021.25 \leq t \end{cases}. \quad (\text{S83})$$

684 For all simulations, we truncated the time series from the beginning of 2014 to the  
685 end of 2023 and aggregated them into weekly cases.

686 To infer intrinsic resilience from time series, we fitted a simple discrete time,  
687 deterministic SIRS model in a Bayesian framework [4]:

$$\Delta t = 1 \text{ week} \quad (\text{S84})$$

$$\text{FOI}(t) = \beta(t)(I(t - \Delta t) + \omega)/N \quad (\text{S85})$$

$$\Delta S(t) = [1 - \exp(-(\text{FOI}(t) + \mu)\Delta t)] S(t - \Delta t) \quad (\text{S86})$$

$$N_{SI}(t) = \frac{\text{FOI}(t)\Delta S(t)}{\text{FOI}(t) + \mu} \quad (\text{S87})$$

$$\Delta I(t) = [1 - \exp(-(\gamma + \mu)\Delta t)] I(t - \Delta t) \quad (\text{S88})$$

$$N_{IR}(t) = \frac{\gamma \Delta I(t)}{\gamma + \mu} \quad (\text{S89})$$

$$\Delta R(t) = [1 - \exp(-(\nu + \mu)\Delta t)] R(t - \Delta t) \quad (\text{S90})$$

$$N_{RS}(t) = \frac{\nu \Delta R(t)}{\nu + \mu} \quad (\text{S91})$$

$$S(t) = S(t - \Delta t) + \mu S - \Delta S(t) + N_{RS}(t) \quad (\text{S92})$$

$$I(t) = I(t - \Delta t) - \Delta I(t) + N_{SI}(t) \quad (\text{S93})$$

$$R(t) = R(t - \Delta t) - \Delta R(t) + N_{IR}(t) \quad (\text{S94})$$

688 where we include an extra term  $\omega$  to account for importation. Although actual  
689 simulations did not include any importation, we had found that including this term  
690 generally helped with model convergence in previous analyses [4]. The transmission  
691 rate was divided into a seasonal term  $\beta_{\text{seas}}(t)$  (repeated every year) and intervention  
692 term  $\alpha(t)$ , which were estimated jointly:

$$\beta(t) = \beta_{\text{seas}}(t)\alpha(t), \quad (\text{S95})$$

693 where  $\alpha < 1$  corresponds to reduction in transmission due to intervention effects. To  
694 constrain the smoothness of  $\beta_{\text{seas}}(t)$ , we imposed cyclic, random-walk priors:

$$\beta_{\text{seas}}(t) \sim \text{Normal}(\beta_{\text{seas}}(t - 1), \sigma) \quad t = 2 \dots 52 \quad (\text{S96})$$

$$\beta_{\text{seas}}(1) \sim \text{Normal}(\beta_{\text{seas}}(52), \sigma) \quad (\text{S97})$$

695 We fixed  $\alpha(t) = 1$  for all  $t < 2020$  and estimate  $\alpha$  assuming a normal prior:

$$\alpha \sim \text{Normal}(1, 0.25). \quad (\text{S98})$$

696 We assumed weakly informative priors on  $\omega$  and  $\nu$ :

$$\omega \sim \text{Normal}(0, 200) \quad (\text{S99})$$

$$\nu \sim \text{Normal}(104, 26) \quad (\text{S100})$$

697 We assumed that the true birth/death rates, population sizes, and recovery rates are  
698 known. We note, however, that assuming  $\gamma = 1/\text{week}$  actually corresponds to a mean  
699 simulated infectious period of 1.6 weeks, which is much longer than the true value;  
700 this approximation allows us to test whether we can still robustly estimate the in-  
701trinsic resilience given parameter mis-specification. Initial conditions were estimated  
702with following priors:

$$S(0) = Ns(0) \quad (\text{S101})$$

$$I(0) = Ni(0) \quad (\text{S102})$$

$$s(0) \sim \text{Uniform}(0, 1) \quad (\text{S103})$$

$$i(0) \sim \text{Half-Normal}(0, 0.001) \quad (\text{S104})$$

703 Finally, the observation model was specified as follows:

$$\text{Cases}(t) \sim \text{Negative-Binomial}(\rho N_{SI}(t), \phi) \quad (\text{S105})$$

$$\rho \sim \text{Half-Normal}(0, 0.02) \quad (\text{S106})$$

$$\phi \sim \text{Half-Normal}(0, 10) \quad (\text{S107})$$

704 where  $\rho$  represents the reporting probability and  $\phi$  represents the negative binomial  
705 overdispersion parameter.

706 The model was fitted to four separate time series: (1) incidence time series from  
707 the SIRS model, (2) incidence time series for strain 1 from the two-strain model,  
708 (3) incidence time series for strain 2 from the two-strain model, and (4) combined  
709 incidence time series for strains 1 and 2 from the two-strain model. The model was  
710 fitted using rstan [37, 38]. The resulting posterior distribution was used to calculate  
711 the intrinsic resilience of the seasonally unforced system with the same parameters;  
712 eigenvalues of the discrete-time SIR model were computed by numerically finding  
713 the equilibrium and calculating the Jacobian matrix.

## 714 **Validations for window-selection criteria**

715 We used stochastic SIRS simulations to identify optimal parameters for the window-  
716 selection criteria that we used for the linear regression for estimating empirical re-  
717silience. For each simulation, we began by generating a random perturbation  $\alpha(t)$   
718from a random set of parameters. First, we drew the duration of perturbation  $\tau_{\text{np}}^i$

719 from a uniform distribution between 1 and 2 years. Then, we drew independent  
 720 normal variables  $z_i$  of length  $\lfloor 364\tau_{\text{np}} \rfloor$  with a standard deviation of 0.02 and took a  
 721 reverse cumulative sum to obtain a realistic shape for the perturbation:

$$x_n = 1 + \sum_{i=n}^{\lfloor 364\tau_{\text{np}} \rfloor} z_i, \quad n = 1, \dots, \lfloor 364\tau_{\text{np}} \rfloor. \quad (\text{S108})$$

722 We repeated this random generation process until less than 10% of  $x_n$  exceeds 1—this  
 723 was done to ensure the perturbation term  $\alpha(t)$  stays below 1 (and therefore reduce  
 724 transmission) for the most part. Then, we set any values that are above 1 or below 0  
 725 to 1 and 0, respectively. Then, we randomly drew the minimum transmission during  
 726 perturbation  $\alpha_{\min}$  from a uniform distribution between 0.5 and 0.7 and scale  $x_n$  to  
 727 have a minimum of  $\alpha_{\min}$ :

$$x_{\text{scale},n} = \alpha_{\min} + (1 - \alpha_{\min}) \times \frac{x_n - \min x_n}{1 - \min x_n}. \quad (\text{S109})$$

728 This allowed us to simulate a realistically shaped perturbation:

$$\alpha(t) = \begin{cases} 1 & t < 2020 \\ x_{\text{scale},364(t-2020)} & 2020 \leq t < 2020 + \tau_{\text{np}} \\ 1 & \tau_{\text{np}} \leq t \end{cases}. \quad (\text{S110})$$

729 Given this perturbation function, we draw  $\mathcal{R}_0$  from a uniform distribution between  
 730 1.5 and 4 and the mean duration of immunity  $1/\delta$  from a uniform distribution be-  
 731 tween 1 and 4. Then, we simulate the stochastic SIRS model from  $S(0) = 10^8/\mathcal{R}_0$   
 732 and  $I(0) = 100$  from 1990 to 2025 and truncate the time series to 2014–2025; if the  
 733 epidemic becomes extinct before the end of simulation, we discard that simulation  
 734 and start over from the perturbation generation step.

735 For each epidemic simulation, we computed the empirical resilience by varying  
 736 the threshold  $R$  for the nearest neighbor approach from 4 to 14 with increments of  
 737 2, the number of divisions  $K$  for the window selection between 8 and 25, and the  
 738 truncation threshold  $a$  for the window selection between 1 to 3; this was done for all  
 739 possible combinations of  $R$ ,  $K$ , and  $a$ . We also compared this with the naive approach  
 740 that uses the entire distance-from-attractor time series, starting from the maximum  
 741 distance to the end of the time series. We repeated this procedure 500 times and  
 742 quantified the correlation between empirical and intrinsic resilience estimates across  
 743 two approaches.

# Supplementary Figures

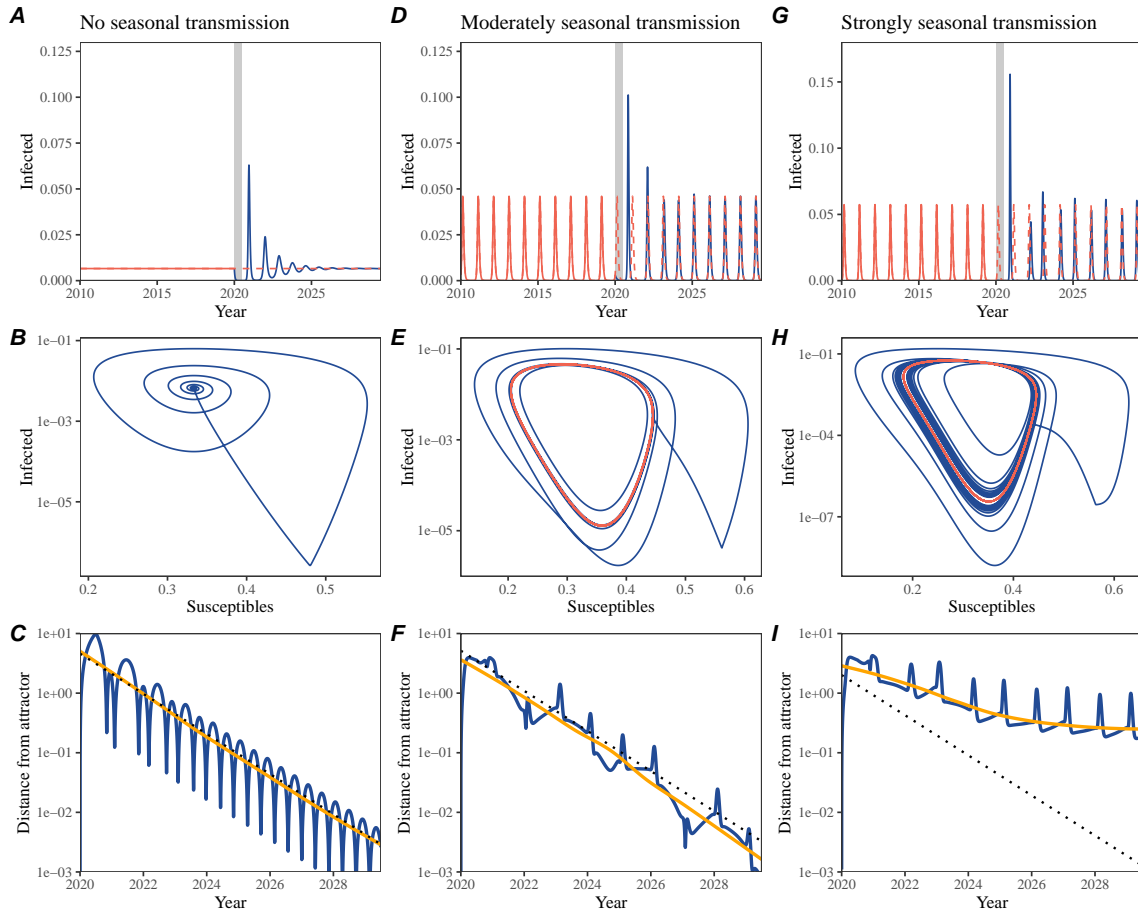


**Figure S1: Impact of seasonal transmission on pathogen resilience.** (A, D, G) Simulated epidemic trajectories using the SIRS model without seasonal forcing (A), with seasonal forcing of amplitude of 0.2 (D), and with seasonal forcing of amplitude of 0.4 (G). Red and blue solid lines represent epidemic dynamics before and after interventions are introduced, respectively. Red dashed lines represent counterfactual epidemic dynamics in the absence of interventions. Gray regions indicate the duration of interventions. (B, E, H) Phase plane representation of the time series in panels A, D, and G alongside the corresponding susceptible host dynamics. Red and blue solid lines represent epidemic trajectories on an SI phase plane before and after interventions are introduced, respectively. (C, F, I) Changes in logged distance from the attractor over time. Blue lines represent the logged distance from the attractor. Orange lines represent the locally estimated scatterplot smoothing (LOESS) fits to the logged distance from the attractor. Dotted lines show the intrinsic resilience of the seasonally unforced system.

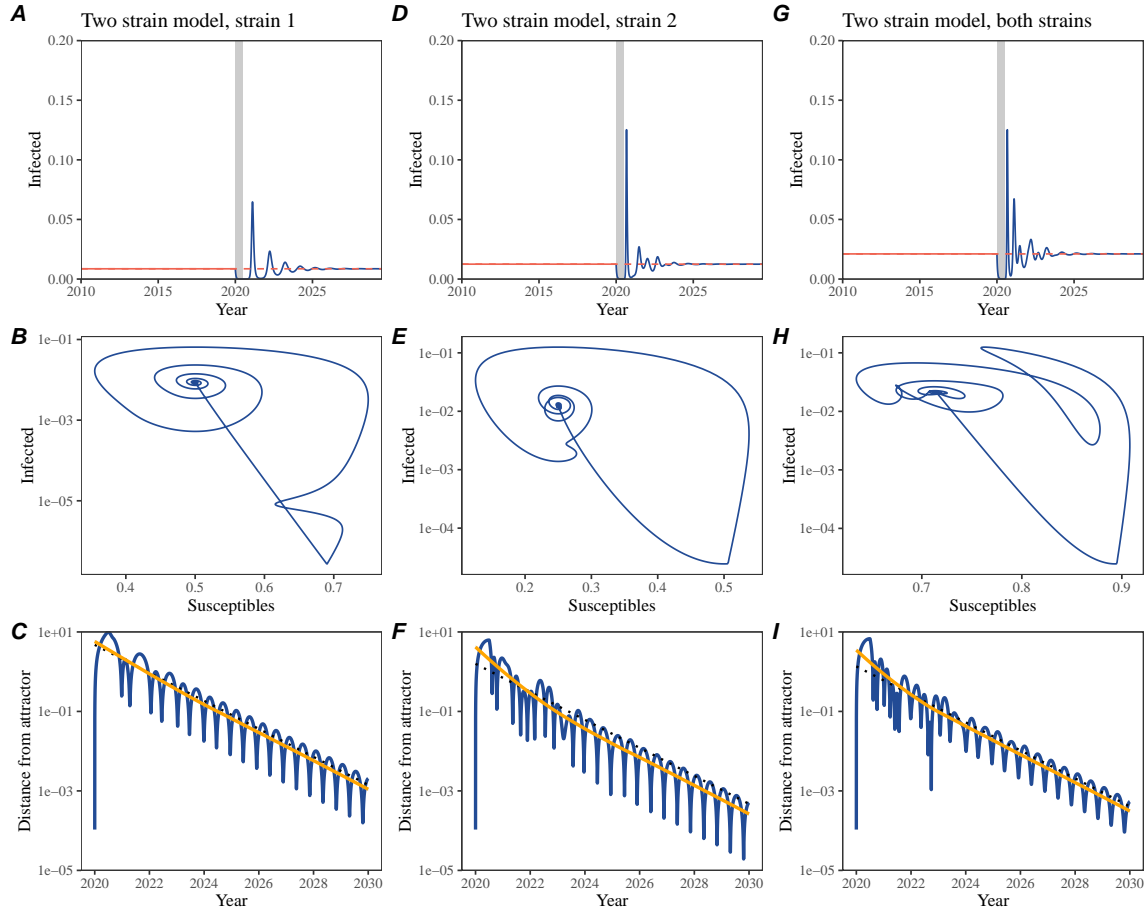


**Figure S2: A simple method to measure pathogen resilience following pandemic perturbations for a two-strain competition system without seasonal forcing.** (A, D, G) Simulated epidemic trajectories using a two-strain system without seasonal forcing. In this model, two strains compete through cross immunity. Red and blue solid lines represent epidemic dynamics before and after interventions are introduced, respectively. Red dashed lines represent counterfactual epidemic dynamics in the absence of interventions. Gray regions indicate the duration of interventions. (B, E, H) Phase plane representation of the time series in panels A, D, and G alongside the corresponding susceptible host dynamics. Blue solid lines represent epidemic trajectories on an SI phase plane before and after interventions are introduced, respectively. (C, F, I) Changes in logged distance from the attractor over time. Blue lines represent the logged distance from the attractor. Orange lines represent the locally estimated scatterplot smoothing (LOESS) fits to the logged distance from the attractor. Dotted lines show the intrinsic resilience of the seasonally unforced system.

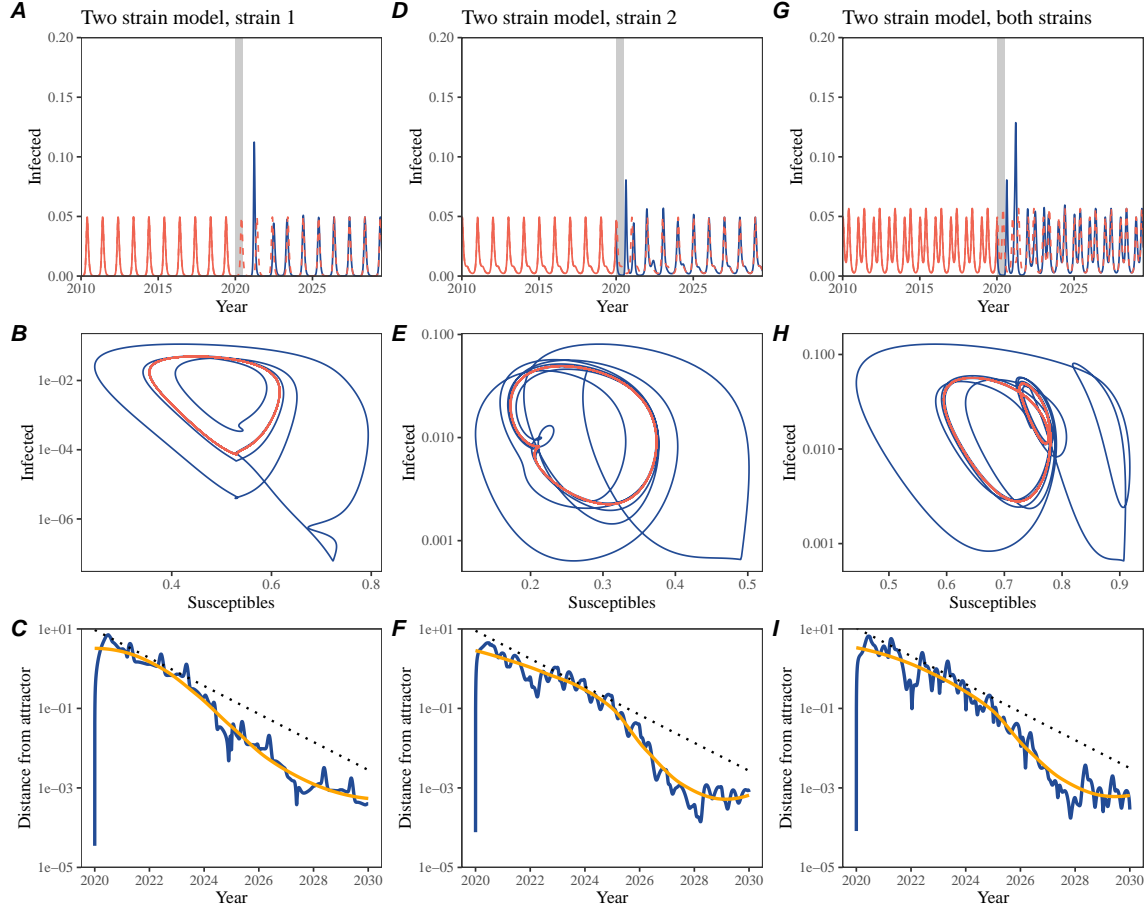


**Figure S3: A simple method to measure pathogen resilience following pandemic perturbations for a two-strain competition system with seasonal forcing.** (A, D, G) Simulated epidemic trajectories using a two-strain system with seasonal forcing (amplitude of 0.2). In this model, two strains compete through cross immunity. Red and blue solid lines represent epidemic dynamics before and after interventions are introduced, respectively. Red dashed lines represent counterfactual epidemic dynamics in the absence of interventions. Gray regions indicate the duration of interventions. (B, E, H) Phase plane representation of the time series in panels A, D, and G alongside the corresponding susceptible host dynamics. Red and blue solid lines represent epidemic trajectories on an SI phase plane before and after interventions are introduced, respectively. (C, F, I) Changes in logged distance from the attractor over time. Blue lines represent the logged distance from the attractor. Orange lines represent the locally estimated scatterplot smoothing (LOESS) fits to the logged distance from the attractor. Dotted lines show the intrinsic resilience of the seasonally unforced system.

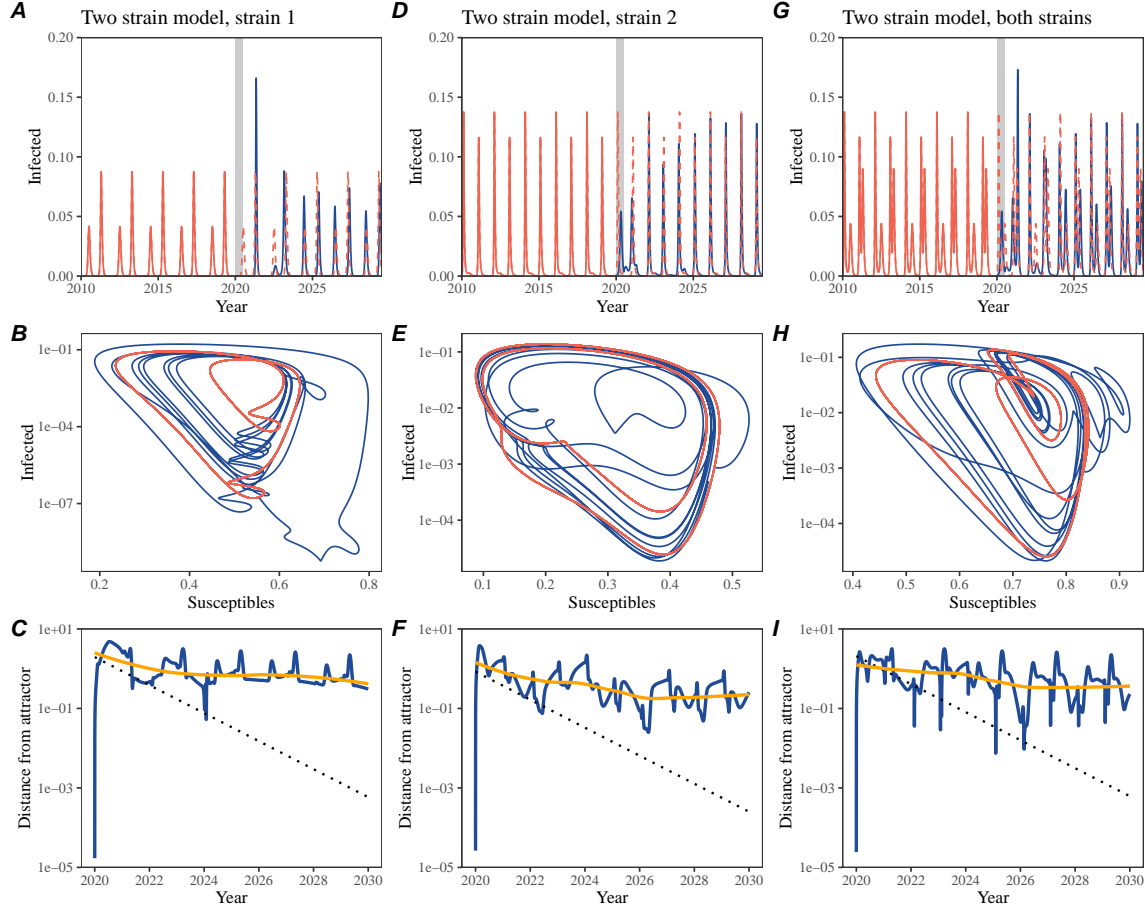


**Figure S4: A simple method to measure pathogen resilience following pandemic perturbations for a multi-strain competition system with strong seasonal forcing.** (A, D, G) Simulated epidemic trajectories using a two-strain system with seasonal forcing (amplitude of 0.2). In this model, two strains compete through cross immunity. Red and blue solid lines represent epidemic dynamics before and after interventions are introduced, respectively. Red dashed lines represent counterfactual epidemic dynamics in the absence of interventions. Gray regions indicate the duration of interventions. (B, E, H) Phase plane representation of the time series in panels A, D, and G alongside the corresponding susceptible host dynamics. Red and blue solid lines represent epidemic trajectories on an SI phase plane before and after interventions are introduced, respectively. (C, F, I) Changes in logged distance from the attractor over time. Blue lines represent the logged distance from the attractor. Orange lines represent the locally estimated scatterplot smoothing (LOESS) fits to the logged distance from the attractor. Dotted lines show the intrinsic resilience of the seasonally unforced system.

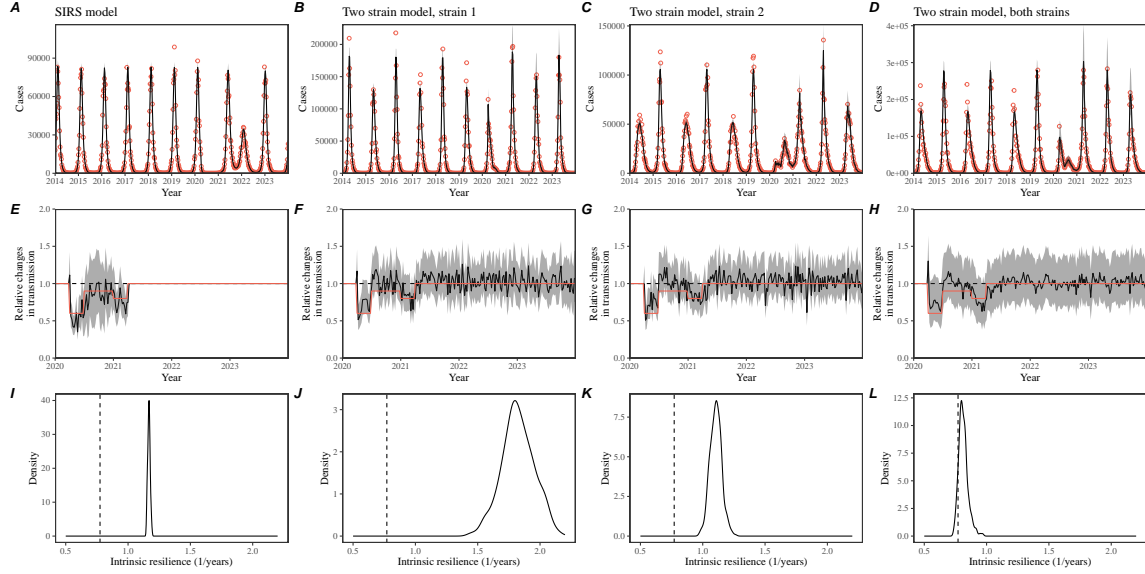


**Figure S5: Mechanistic model fits to simulated data and inferred intrinsic resilience.** We simulated discrete time, stochastic epidemic trajectories using a seasonally forced SIRS model (A,E,I) and a seasonally forced two-strain model (B–D, F–H, and J–L) and tested whether we can estimate the intrinsic resilience of the seasonally unforced versions of the model by fitting a mechanistic model (Supplementary Text). We fitted the same discrete time, one strain, deterministic SIRS model in each scenario. (A–D) Simulated case time series from corresponding models shown in the title (red) and SIRS model fits (black). (E–H) Assumed changes in transmission due to pandemic perturbations (red) and estimated time-varying relative transmission rates for the perturbation impact from the SIRS model fits (black). Solid lines and shaded regions represent fitted posterior median and 95% credible intervals. (I–L) Comparisons between the true and estimated intrinsic resilience of the seasonally unforced system. Vertical lines represent the true intrinsic resilience of the seasonally unforced system. Density plots represent the posterior distribution of the inferred intrinsic resilience of the seasonally unforced SIRS model using fitted parameters.

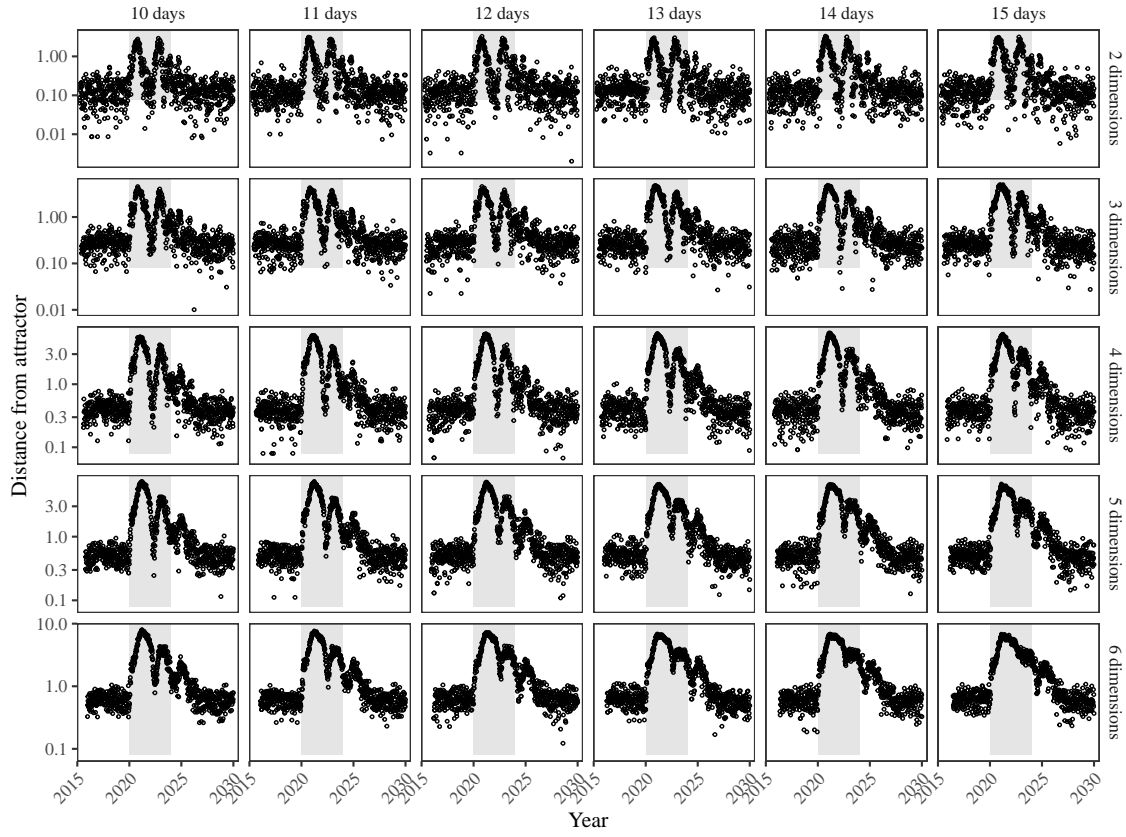


**Figure S6: Sensitivity of the distance from the attractor to choice of embedding lags and dimensions.** Sensitivity analysis for the distance-from-attractor time series shown in Figure 3E in the main text by varying the embedding lag between 10–15 days and embedding dimensions between 2–6 dimensions. The gray region represents the assumed period of pandemic perturbation.

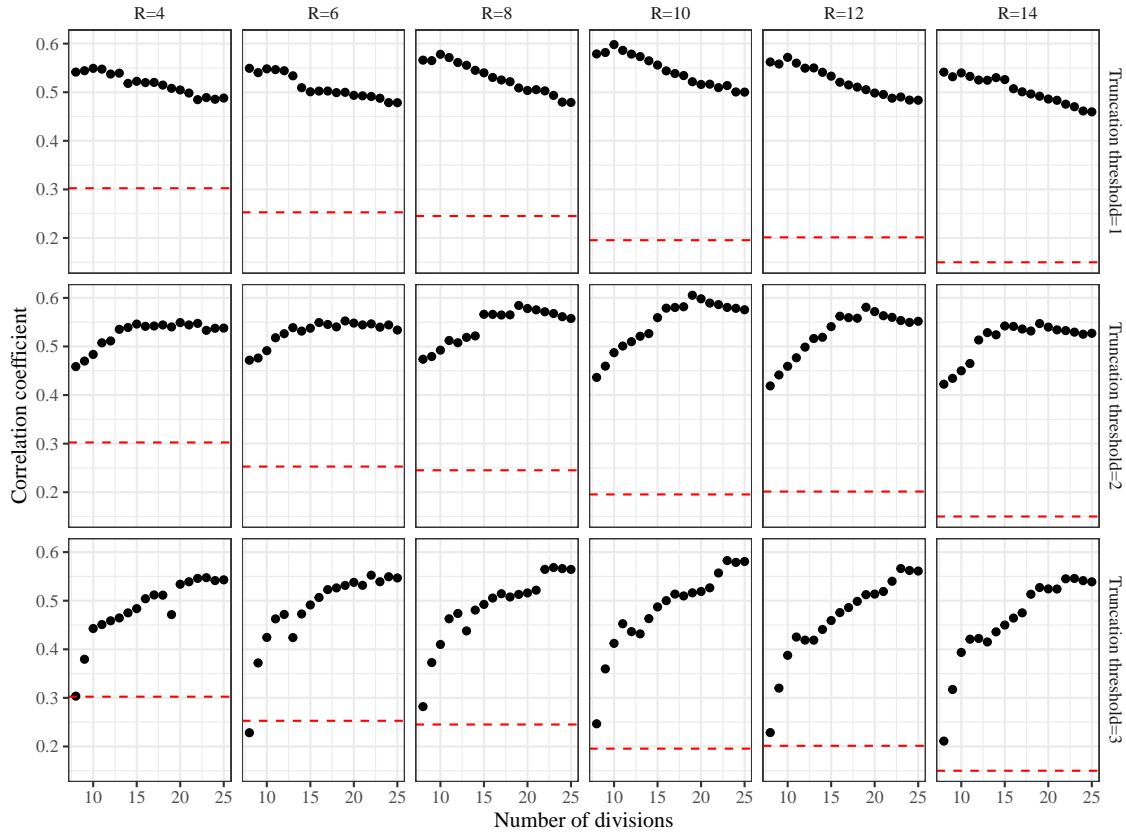


**Figure S7: Impact of fitting window selection on the estimation of empirical resilience.** We simulated 500 epidemics of a stochastic SIRS model with randomly drawn parameters and randomly generated pandemic perturbations (Supplementary Text). For each simulation, we varied the false nearest neighbor threshold  $R$  for reconstructing the empirical attractor as well as the parameters for regression window selection (i.e., the truncation threshold  $a$  and the number of divisions  $K$ ). Each point represents the resulting correlation coefficient between empirical and intrinsic resilience estimates for a given scenario. Dashed lines represent the correlation coefficient between empirical and intrinsic resilience estimates for the naive approach that fits a linear regression on a log scale, starting from the maximum distance until the end of the time series.

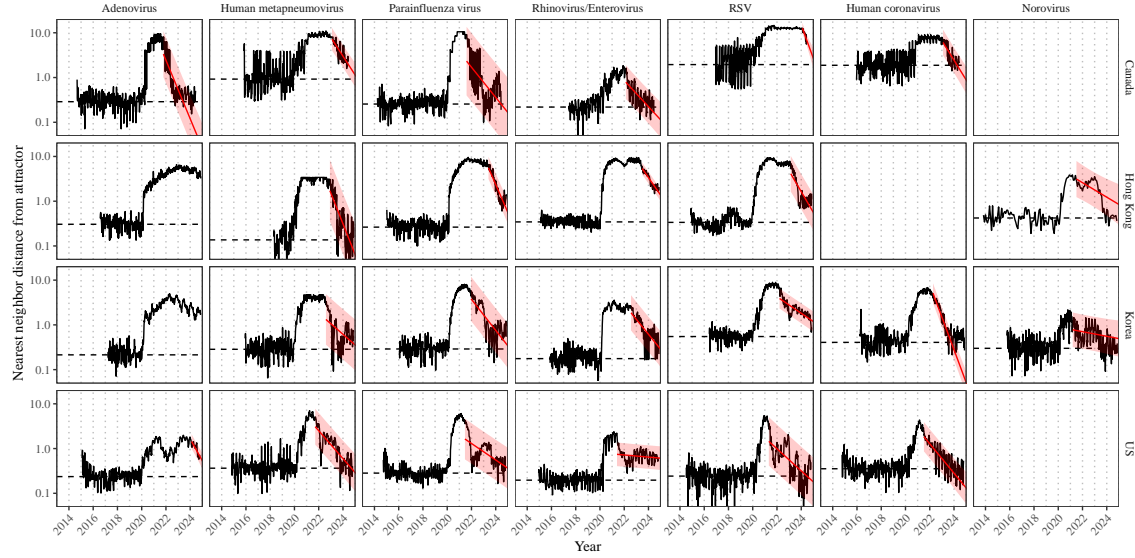


**Figure S8: Estimated time series of distance from the attractor for each pathogen and corresponding linear regression fits using automated window selection criterion across Canada, Hong Kong, Korea, and the US.** Black lines represent the estimated distance from the attractor. Red lines and shaded regions represent the linear regression fits and corresponding 95% confidence intervals. Dashed lines represent the average of the pre-pandemic nearest neighbor distances.

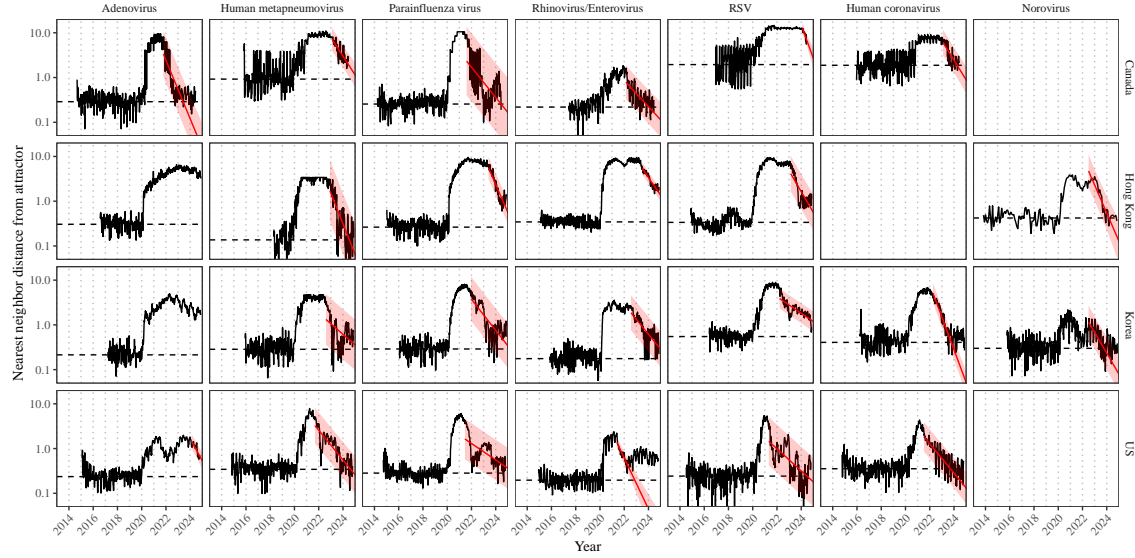


**Figure S9: Estimated time series of distance from the attractor for each pathogen and corresponding linear regression fits across Canada, Hong Kong, Korea, and the US, including ad-hoc regression window selection.** We used ad-hoc regression windows for norovirus in Hong Kong and Korea and rhinovirus/enterovirus in the US. Black lines represent the estimated distance from the attractor. Red lines and shaded regions represent the linear regression fits and corresponding 95% confidence intervals. Dashed lines represent the average of the pre-pandemic nearest neighbor distances.

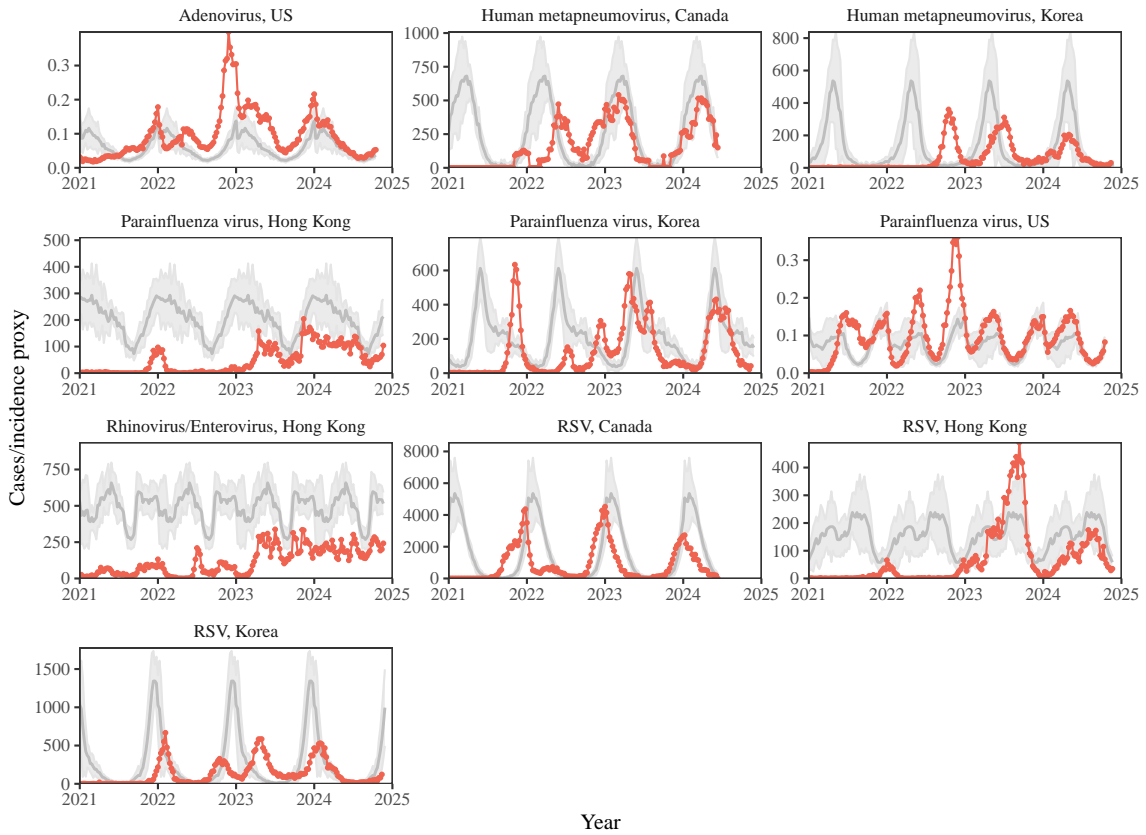


**Figure S10: Observed dynamics for pathogen that are predicted to return after the end of 2024.** Red points and lines represent data before 2020. Gray lines and shaded regions represent the mean seasonal patterns and corresponding 95% confidence intervals around the mean, previously shown in Figure 1.

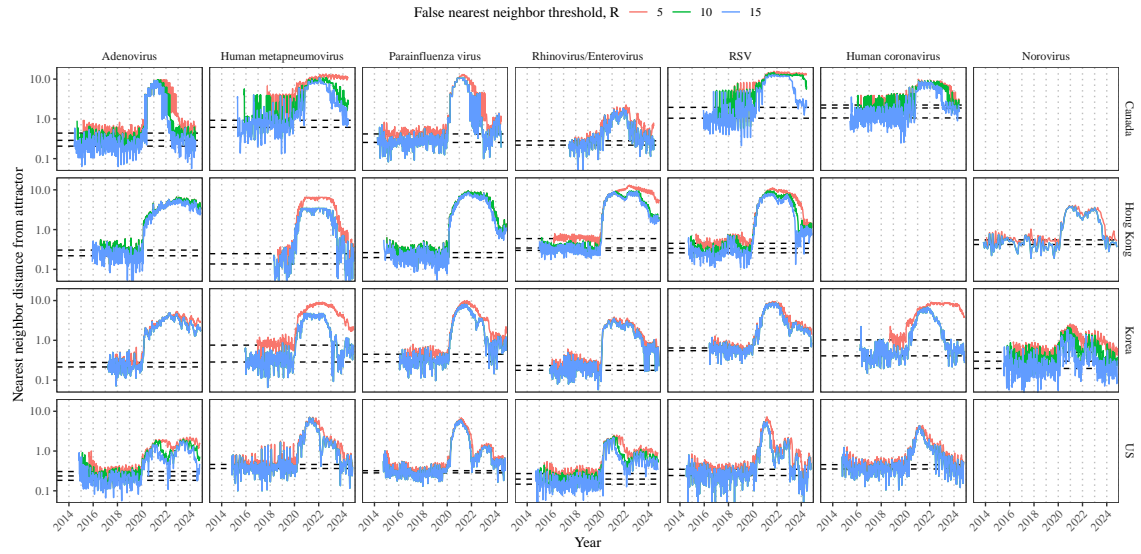


**Figure S11: Estimated time series of distance from the attractor for each pathogen across different choices about false nearest neighbor threshold values.** Using higher threshold values for the false nearest neighbor approach gives lower embedding dimensions. Colored lines represent the estimated distance from the attractor for different threshold values.

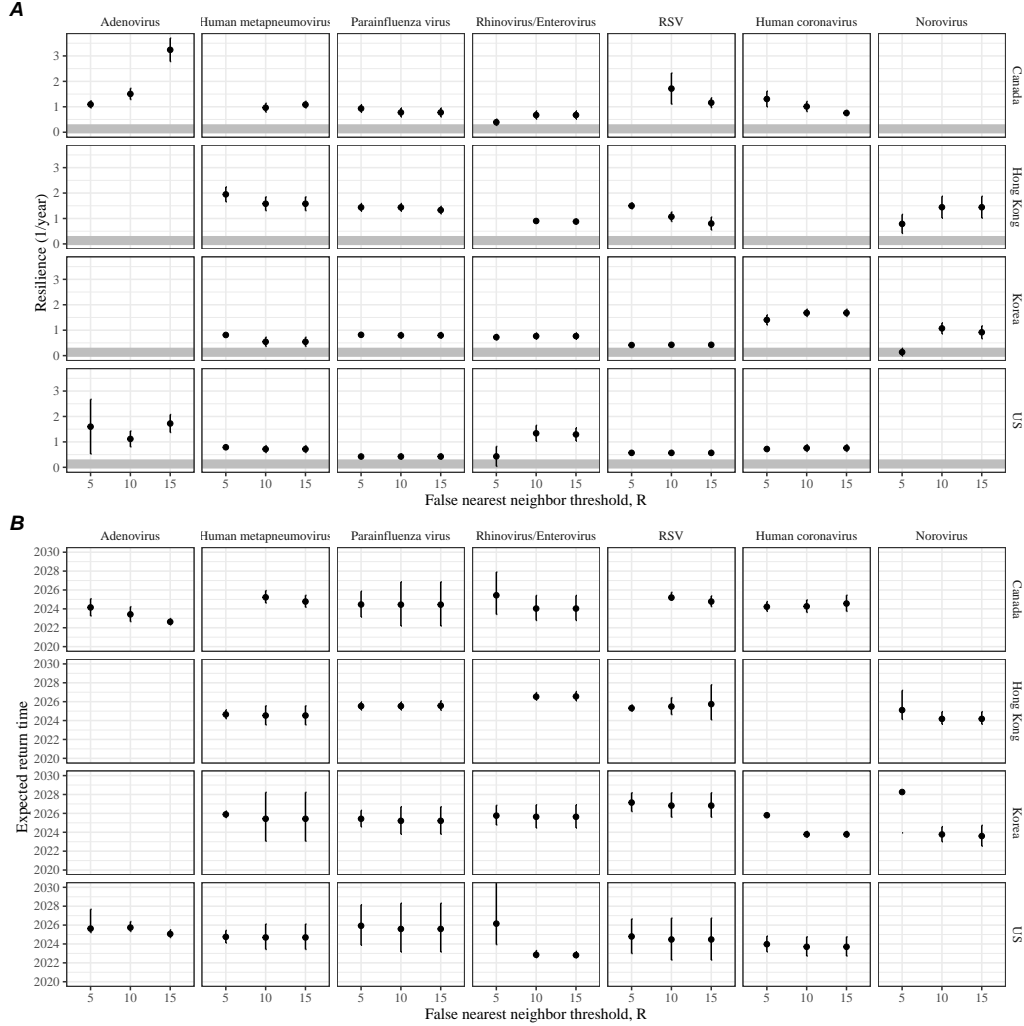


**Figure S12: Summary of resilience estimates and predictions for return time across different choices about false nearest neighbor threshold values.** The automated window selection method was used for all scenarios to estimate pathogen resilience, except for norovirus in Hong Kong and Korea and rhinovirus/enterovirus in the US. We used the same ad-hoc regression windows for norovirus in Hong Kong and Korea and rhinovirus/enterovirus in the US as we did in the main analysis. (A) Estimated pathogen resilience. The gray horizontal line represents the intrinsic resilience of pre-vaccination measles dynamics. (B) Predicted timing of when each pathogen will return to their pre-pandemic cycles. The dashed line in panel B indicates the end of 2024. Error bars represent 95% confidence intervals.

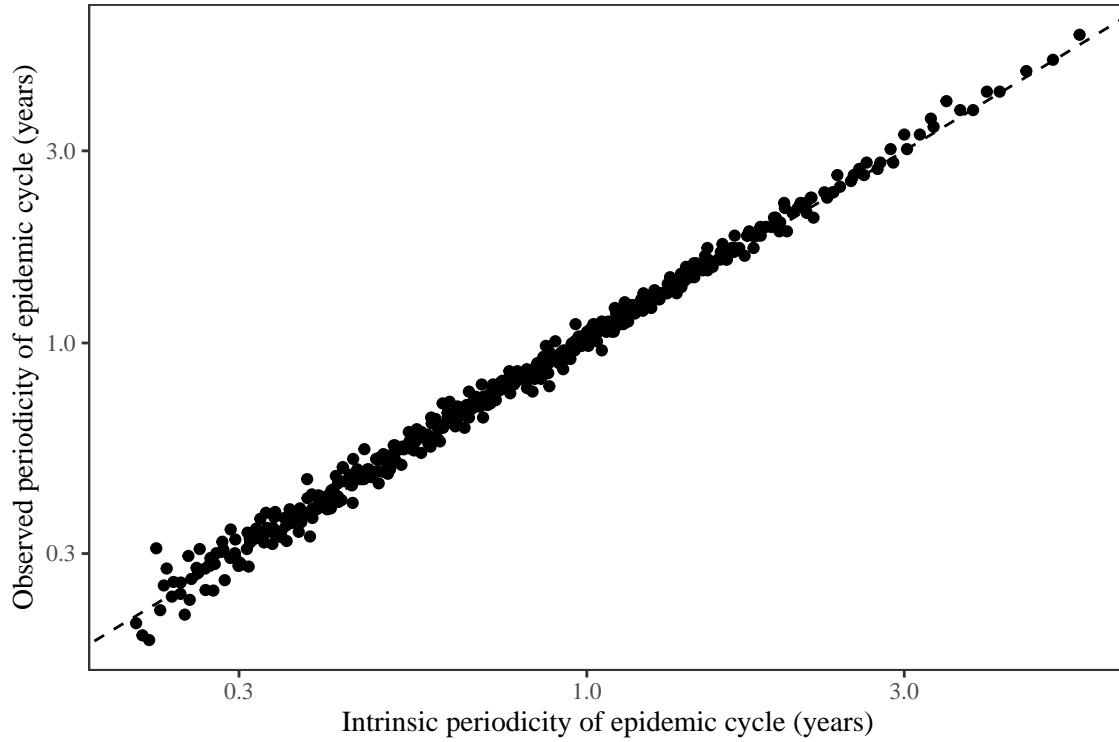


Figure S13: **Comparison between the observed and intrinsic periodicity of the epidemic cycle of the seasonally unforced SIRS model.** The observed periodicity of the epidemic corresponds to the periodicity at which maximum spectral density occurs. The intrinsic periodicity of the epidemic corresponds to  $2\pi/\text{Im}(\lambda)$ , where  $\text{Im}(\lambda)$  is the imaginary part of the eigenvalue.

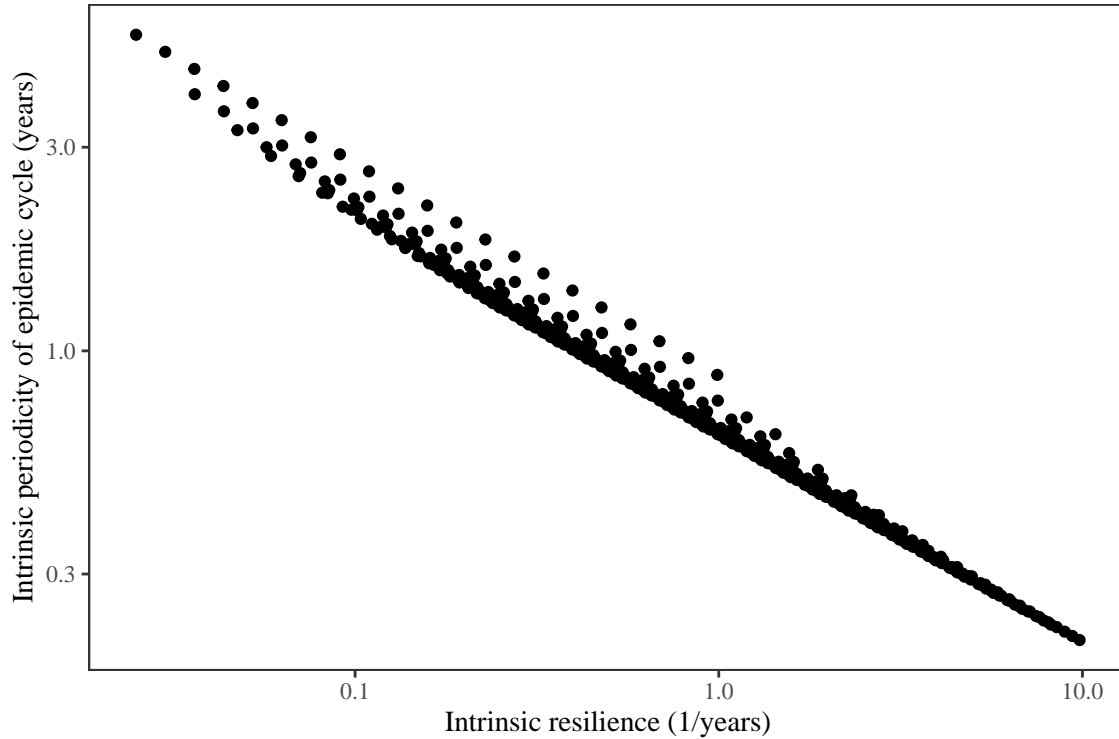


Figure S14: **Comparison between the intrinsic resilience and periodicity of the epidemic cycle of the seasonally unforced SIRS model.** The intrinsic resilience of the epidemic corresponds to the negative of the real value of the eigenvalue  $-\text{Re}(\lambda)$ . The intrinsic periodicity of the epidemic corresponds to  $2\pi/\text{Im}(\lambda)$ , where  $\text{Im}(\lambda)$  is the imaginary part of the eigenvalue.

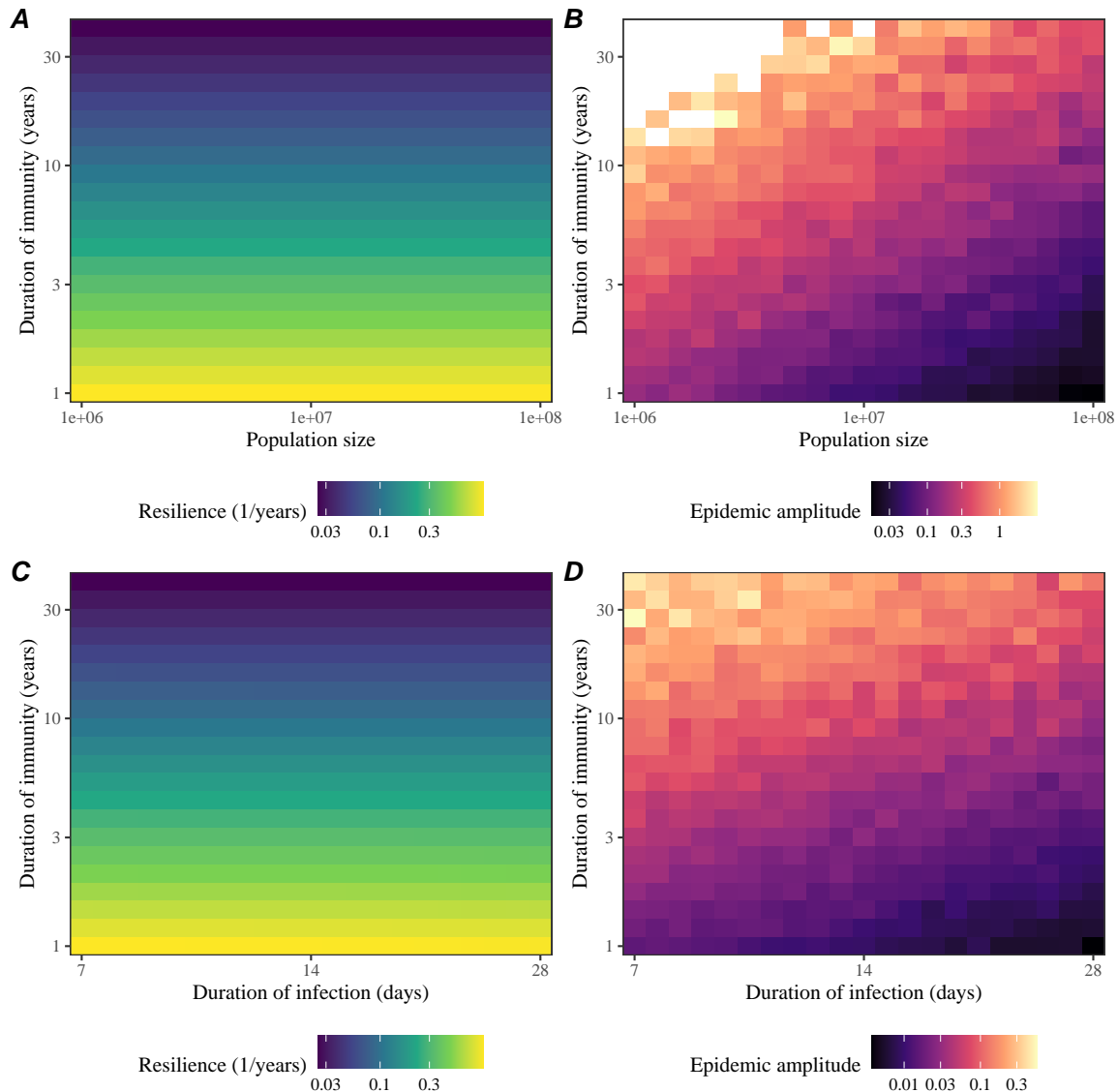
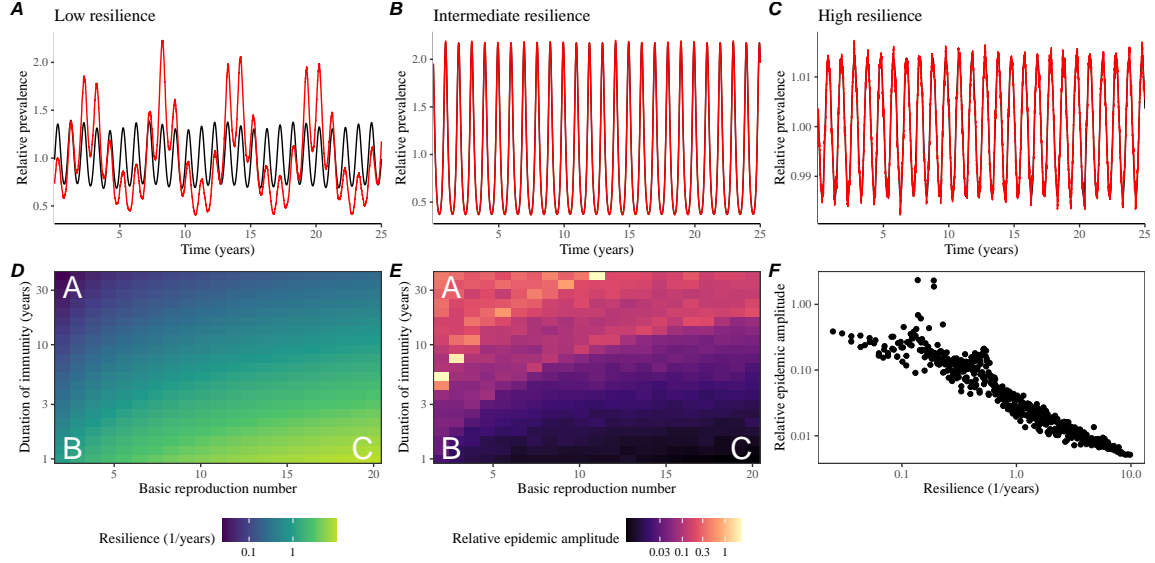


Figure S15: **Impact of population size and the average duration of infection of a host-pathogen system to its sensitivity to stochastic perturbations.** (A) Intrinsic resilience of a system as a function of population size and the average duration of immunity. (B) Epidemic amplitude as a function of population size and the average duration of immunity. (C) Intrinsic resilience of a system as a function of the average duration of infection and the average duration of immunity. (D) Epidemic amplitude as a function of the average duration of infection and the average duration of immunity. The epidemic amplitude corresponds to  $(\max I - \min I)/(2\bar{I})$ , where  $\bar{I}$  represents the mean prevalence.



**Figure S16: Linking resilience of a host-pathogen system to its sensitivity to stochastic perturbations for the seasonally forced SIRS model.** (A–C) Epidemic trajectories of a stochastic SIRS model with demographic stochasticity across three different resilience values: low, intermediate, and high. The relative prevalence was calculated by dividing infection prevalence by its mean value. Black lines represent deterministic epidemic trajectories. Red lines represent stochastic epidemic trajectories. (D) The intrinsic resilience of the seasonally unforced system as a function of the basic reproduction number  $\mathcal{R}_0$  and the duration of immunity. (E) The relative epidemic amplitude, a measure of sensitivity to stochastic perturbations, as a function of the basic reproduction number  $\mathcal{R}_0$  and the duration of immunity. To calculate the relative epidemic amplitude, we first take the relative difference in infection prevalence between stochastic and deterministic trajectories:  $\epsilon = (I_{\text{stoch}} - I_{\text{det}})/I_{\text{det}}$ . Then, we calculate the difference between maximum and minimum of the relative difference and divide by half:  $(\max \epsilon - \min \epsilon)/2$ . Labels A–C in panels D and E correspond to scenarios shown in panels A–C. (F) The relationship between pathogen resilience and relative epidemic amplitude.

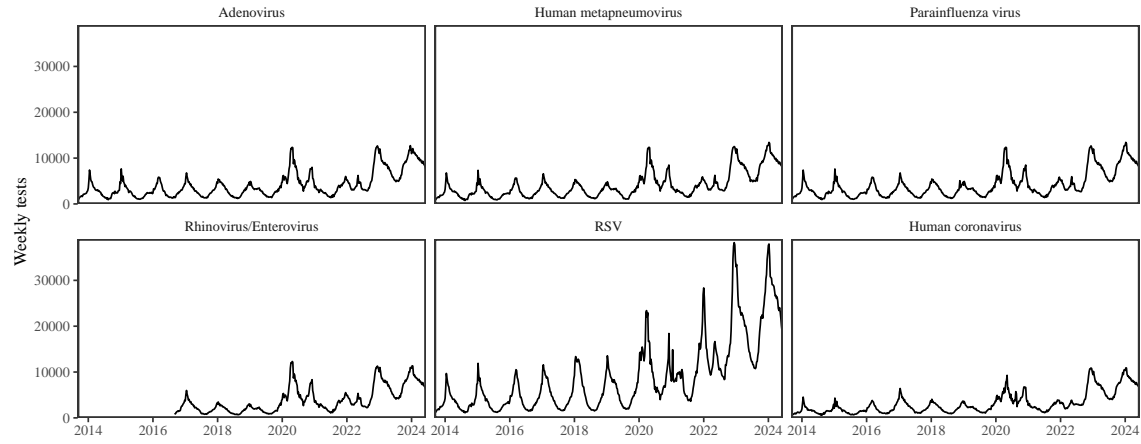


Figure S17: Testing patterns for respiratory pathogens in Canada.

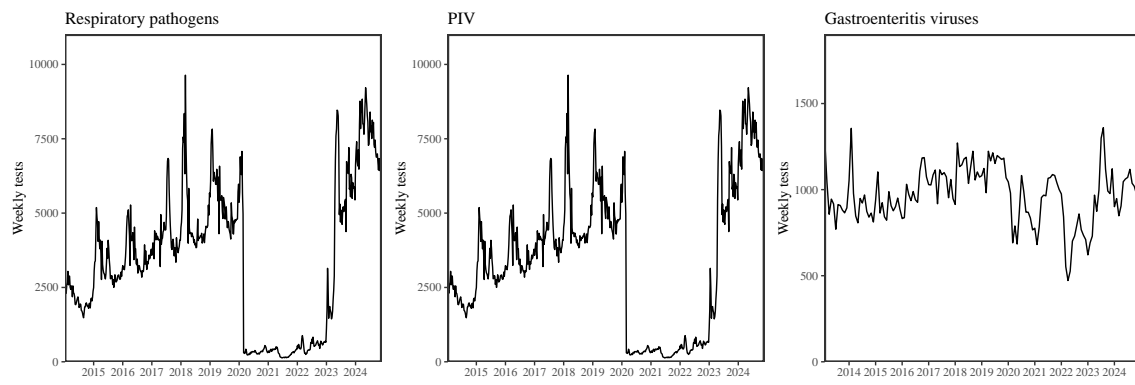


Figure S18: Testing patterns for respiratory pathogens, PIV, and gastroenteritis viruses in Hong Kong.

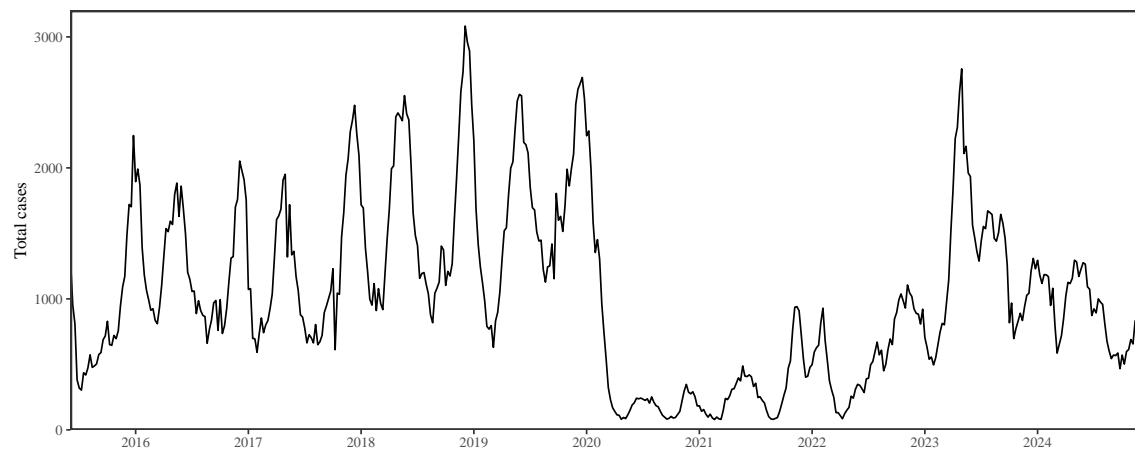


Figure S19: Total number of reported respiratory infection cases in Korea.

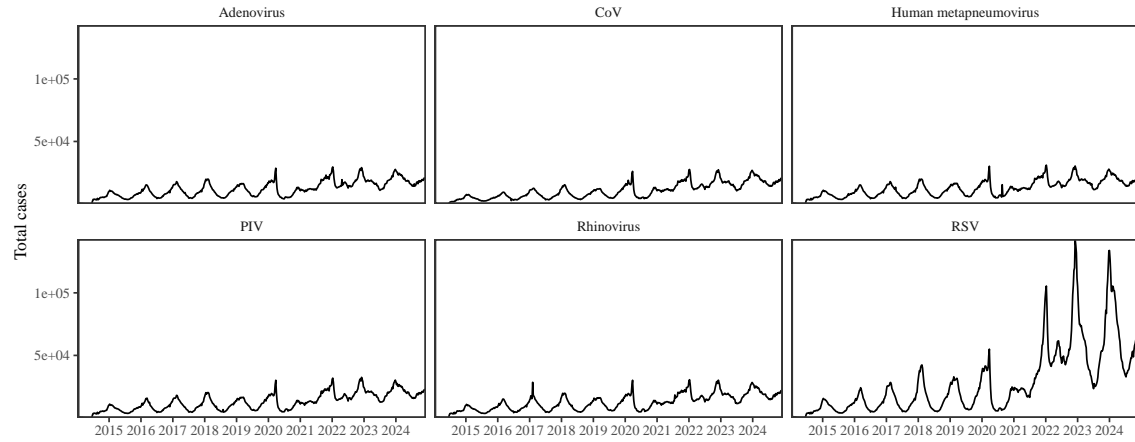


Figure S20: Testing patterns for respiratory pathogens in the US reported through the NREVSS.

745    **References**

- 746 [1] Rachel E Baker, Sang Woo Park, Wenchang Yang, Gabriel A Vecchi, C Jessica E  
747 Metcalf, and Bryan T Grenfell. The impact of COVID-19 nonpharmaceutical  
748 interventions on the future dynamics of endemic infections. *Proceedings of the*  
749 *National Academy of Sciences*, 117(48):30547–30553, 2020.
- 750 [2] Gabriela B Gomez, Cedric Mahé, and Sandra S Chaves. Uncertain effects of the  
751 pandemic on respiratory viruses. *Science*, 372(6546):1043–1044, 2021.
- 752 [3] Mihaly Koltai, Fabienne Krauer, David Hodgson, Edwin van Leeuwen, Marina  
753 Treskova-Schwarzbach, Mark Jit, and Stefan Flasche. Determinants of RSV  
754 epidemiology following suppression through pandemic contact restrictions. *Epi-*  
755 *demics*, 40:100614, 2022.
- 756 [4] Sang Woo Park, Brooklyn Noble, Emily Howerton, Bjarke F Nielsen, Sarah  
757 Lentz, Lilliam Ambroggio, Samuel Dominguez, Kevin Messacar, and Bryan T  
758 Grenfell. Predicting the impact of non-pharmaceutical interventions against  
759 COVID-19 on *Mycoplasma pneumoniae* in the United States. *Epidemics*,  
760 49:100808, 2024.
- 761 [5] Amanda C Perofsky, Chelsea L Hansen, Roy Burstein, Shanda Boyle, Robin  
762 Prentice, Cooper Marshall, David Reinhart, Ben Capodanno, Melissa Truong,  
763 Kristen Schwabe-Fry, et al. Impacts of human mobility on the citywide trans-  
764 mission dynamics of 18 respiratory viruses in pre-and post-COVID-19 pandemic  
765 years. *Nature communications*, 15(1):4164, 2024.
- 766 [6] Eric J Chow, Timothy M Uyeki, and Helen Y Chu. The effects of the COVID-19  
767 pandemic on community respiratory virus activity. *Nature Reviews Microbiol-*  
768 *ogy*, 21(3):195–210, 2023.
- 769 [7] Stephen M Kissler, Christine Tedijanto, Edward Goldstein, Yonatan H Grad,  
770 and Marc Lipsitch. Projecting the transmission dynamics of SARS-CoV-2  
771 through the postpandemic period. *Science*, 368(6493):860–868, 2020.
- 772 [8] Rachel E Baker, Chadi M Saad-Roy, Sang Woo Park, Jeremy Farrar, C Jessica E  
773 Metcalf, and Bryan T Grenfell. Long-term benefits of nonpharmaceutical inter-  
774 ventions for endemic infections are shaped by respiratory pathogen dynamics.  
775 *Proceedings of the National Academy of Sciences*, 119(49):e2208895119, 2022.
- 776 [9] Maaike C Swets, Clark D Russell, Ewen M Harrison, Annemarie B Docherty,  
777 Nazir Lone, Michelle Girvan, Hayley E Hardwick, Leonardus G Visser, Pe-  
778 ter JM Openshaw, Geert H Groeneveld, et al. SARS-CoV-2 co-infection with  
779 influenza viruses, respiratory syncytial virus, or adenoviruses. *The Lancet*,  
780 399(10334):1463–1464, 2022.

- 781 [10] Chun-Yang Lin, Joshua Wolf, David C Brice, Yilun Sun, Macauley Locke,  
782 Sean Cherry, Ashley H Castellaw, Marie Wehenkel, Jeremy Chase Crawford,  
783 Veronika I Zarnitsyna, et al. Pre-existing humoral immunity to human common  
784 cold coronaviruses negatively impacts the protective SARS-CoV-2 antibody re-  
785 sponse. *Cell host & microbe*, 30(1):83–96, 2022.
- 786 [11] Sam M Murray, Azim M Ansari, John Frater, Paul Klenerman, Susanna  
787 Dunachie, Eleanor Barnes, and Ane Ogbe. The impact of pre-existing cross-  
788 reactive immunity on SARS-CoV-2 infection and vaccine responses. *Nature*  
789 *Reviews Immunology*, 23(5):304–316, 2023.
- 790 [12] John-Sebastian Eden, Chisha Sikazwe, Ruopeng Xie, Yi-Mo Deng, Sheena G  
791 Sullivan, Alice Michie, Avram Levy, Elena Cutmore, Christopher C Blyth,  
792 Philip N Britton, et al. Off-season RSV epidemics in Australia after easing  
793 of COVID-19 restrictions. *Nature communications*, 13(1):2884, 2022.
- 794 [13] Stuart L Pimm. The structure of food webs. *Theoretical population biology*,  
795 16(2):144–158, 1979.
- 796 [14] Michael G Neubert and Hal Caswell. Alternatives to resilience for measuring  
797 the responses of ecological systems to perturbations. *Ecology*, 78(3):653–665,  
798 1997.
- 799 [15] Lance H Gunderson. Ecological resilience—in theory and application. *Annual*  
800 *review of ecology and systematics*, 31(1):425–439, 2000.
- 801 [16] Vasilis Dakos and Sonia Kéfi. Ecological resilience: what to measure and how.  
802 *Environmental Research Letters*, 17(4):043003, 2022.
- 803 [17] Floris Takens. Detecting strange attractors in turbulence. In *Dynamical Sys-*  
804 *tems and Turbulence, Warwick 1980: proceedings of a symposium held at the*  
805 *University of Warwick 1979/80*, pages 366–381. Springer, 2006.
- 806 [18] Jonathan Dushoff, Joshua B Plotkin, Simon A Levin, and David JD Earn.  
807 Dynamical resonance can account for seasonality of influenza epidemics. *Pro-*  
808 , 101(48):16915–16916, 2004.
- 809 [19] Alan Hastings, Karen C Abbott, Kim Cuddington, Tessa Francis, Gabriel Gell-  
810 ner, Ying-Cheng Lai, Andrew Morozov, Sergei Petrovskii, Katherine Scran-  
811 ton, and Mary Lou Zeeman. Transient phenomena in ecology. *Science*,  
812 361(6406):eaat6412, 2018.
- 813 [20] Matthew B Kennel, Reggie Brown, and Henry DI Abarbanel. Determining  
814 embedding dimension for phase-space reconstruction using a geometrical con-  
815 struction. *Physical review A*, 45(6):3403, 1992.

- 816 [21] Eugene Tan, Shannon Algar, Débora Corrêa, Michael Small, Thomas Stemler,  
817 and David Walker. Selecting embedding delays: An overview of embedding  
818 techniques and a new method using persistent homology. *Chaos: An Interdis-*  
819 *ciplinary Journal of Nonlinear Science*, 33(3), 2023.
- 820 [22] Jennifer M Radin, Anthony W Hawksworth, Peter E Kammerer, Melinda Bal-  
821 ansay, Rema Raman, Suzanne P Lindsay, and Gary T Brice. Epidemiology  
822 of pathogen-specific respiratory infections among three US populations. *PLoS*  
823 *One*, 9(12):e114871, 2014.
- 824 [23] Guojian Lv, Limei Shi, Yi Liu, Xuecheng Sun, and Kai Mu. Epidemiological  
825 characteristics of common respiratory pathogens in children. *Scientific Reports*,  
826 14(1):16299, 2024.
- 827 [24] Saverio Caini, Adam Meijer, Marta C Nunes, Laetitia Henaff, Malaika Zounon,  
828 Bronke Boudewijns, Marco Del Riccio, and John Paget. Probable extinction of  
829 influenza b/yamagata and its public health implications: a systematic literature  
830 review and assessment of global surveillance databases. *The Lancet Microbe*,  
831 2024.
- 832 [25] Zhiyuan Chen, Joseph L-H Tsui, Bernardo Gutierrez, Simon Busch Moreno,  
833 Louis du Plessis, Xiaowei Deng, Jun Cai, Sumali Bajaj, Marc A Suchard,  
834 Oliver G Pybus, et al. COVID-19 pandemic interventions reshaped the global  
835 dispersal of seasonal influenza viruses. *Science*, 386(6722):eadq3003, 2024.
- 836 [26] Bryan T Grenfell, Ottar N Bjørnstad, and Bärbel F Finkenstädt. Dynamics of  
837 measles epidemics: scaling noise, determinism, and predictability with the TSIR  
838 model. *Ecological monographs*, 72(2):185–202, 2002.
- 839 [27] Samit Bhattacharyya, Per H Gesteland, Kent Korgenski, Ottar N Bjørnstad,  
840 and Frederick R Adler. Cross-immunity between strains explains the dynamical  
841 pattern of paramyxoviruses. *Proceedings of the National Academy of Sciences*,  
842 112(43):13396–13400, 2015.
- 843 [28] Virginia E Pitzer, Cécile Viboud, Vladimir J Alonso, Tanya Wilcox, C Jessica  
844 Metcalf, Claudia A Steiner, Amber K Haynes, and Bryan T Grenfell. Environ-  
845 mental drivers of the spatiotemporal dynamics of respiratory syncytial virus in  
846 the United States. *PLoS pathogens*, 11(1):e1004591, 2015.
- 847 [29] Katharine R Dean, Fabienne Krauer, Lars Walløe, Ole Christian Lingjærde, Bar-  
848 bara Bramanti, Nils Chr Stenseth, and Boris V Schmid. Human ectoparasites  
849 and the spread of plague in Europe during the Second Pandemic. *Proceedings*  
850 *of the National Academy of Sciences*, 115(6):1304–1309, 2018.
- 851 [30] Margarita Pons-Salort and Nicholas C Grassly. Serotype-specific immunity  
852 explains the incidence of diseases caused by human enteroviruses. *Science*,  
853 361(6404):800–803, 2018.

- 854 [31] Sarah Cobey and Edward B Baskerville. Limits to causal inference with state-  
855 space reconstruction for infectious disease. *PLoS one*, 11(12):e0169050, 2016.
- 856 [32] Public Health Agency of Canada. Respiratory virus detections in  
857 Canada. 2024. <https://www.canada.ca/en/public-health/services/surveillance/respiratory-virus-detections-canada.html>. Accessed Sep  
858 4, 2024.
- 860 [33] Centre for Health Protection. Detection of pathogens from respiratory spec-  
861 imens. 2024. <https://www.chp.gov.hk/en/statistics/data/10/641/642/2274.html>. Accessed Nov 20, 2024.
- 863 [34] Centre for Health Protection. Detection of gastroenteritis viruses from faecal  
864 specimens. 2024. <https://www.chp.gov.hk/en/statistics/data/10/641/717/3957.html>. Accessed Nov 20, 2024.
- 866 [35] Korea Disease Control and Prevention Agency. Acute respiratory infection,  
867 Sentinel surveillance infectious diseases. 2024. <https://dportal.kdca.go.kr/pot/is/st/ari.do>. Accessed Nov 20, 2024.
- 869 [36] Edward Goldstein, Sarah Cobey, Saki Takahashi, Joel C Miller, and Marc Lipsitch.  
870 Predicting the epidemic sizes of influenza A/H1N1, A/H3N2, and B: a  
871 statistical method. *PLoS medicine*, 8(7):e1001051, 2011.
- 872 [37] Bob Carpenter, Andrew Gelman, Matthew D Hoffman, Daniel Lee, Ben  
873 Goodrich, Michael Betancourt, Marcus A Brubaker, Jiqiang Guo, Peter Li,  
874 and Allen Riddell. Stan: A probabilistic programming language. *Journal of  
875 statistical software*, 76, 2017.
- 876 [38] Stan Development Team. RStan: the R interface to Stan, 2024. R package  
877 version 2.32.6.